

DESIGN, FABRICATION, AND CHARACTERIZATION OF AN ACTIVELY-CONTROLLED
MACH 5 TO 8 WIND TUNNEL

A Dissertation Proposal

by

JACOB B. VAUGHN

Submitted to the Graduate and Professional School of
Texas A&M University
in partial fulfillment of the requirements for the degree of
DOCTOR OF PHILOSOPHY

Chair of Committee, Edward White

Committee Members, Rodney Bowersox

Nathan Tichenor

Je Han

Head of Department, Ivett Leyva

March 2024

Major Subject: Aerospace Engineering

Copyright 2024 Jacob B. Vaughn

NOMENCLATURE

Acronyms

ACE	Actively Controlled Expansion
AIAA	American Institute of Aeronautics and Astronautics
AGARD	Advisory Group for Aerospace Research and Development
BCDC	Bush Combat Development Complex
CFD	Computational Fluid Dynamics
FEA	Finite Element Analysis
FEDC	Fischer Engineering Design Center
FOS	Factor of safety
HMI	Human Machine Interface
M6QT	Mach 6 Quiet Tunnel
MATLAB	Matrix Laboratory
MDOE	Modern Design of Experiments
MOC	Method of characteristics
NAHL	National Aerothermochemistry and Hypersonics Laboratory
NASA	National Aeronautics and Space Administration
PID	Proportional Integral Derivative
PLC	Programmable Logic Controller
PSIA	Pounds per Square Inch (Absolute)
RMS	Root Mean Squared
US3D	Unstructured 3D CFD

Common Symbols

A	Area
-----	------

A^*	Nozzle throat area
F	...
K	Proportional Gain Constant
M	Mach number
R	Gas constant
Re'	Unit Reynolds number, $\rho U / \mu$
P	Static Pressure
T	Static Temperature
T_d	Derivative Time Constant
T_i	Integral Time Constant
U	Streamwise Velocity
a	Speed of sound
h^*	Nozzle throat height
\dot{m}	Mass flow rate

Greek Symbols

α	Shock angle
ρ	Density
γ	Ratio of specific heats (c_P / c_V)
μ	Dynamic viscosity
θ	Wedge-deflection angle
ξ	Pressure ratio across oblique shock

Common Subscripts

0	Stagnation condition
D	Detachment condition
V	Von Neumann condition

∞

Freestream condition

set

Set condition for PID reference

TABLE OF CONTENTS

	Page
NOMENCLATURE	1
TABLE OF CONTENTS	4
LIST OF FIGURES	6
LIST OF TABLES.....	8
1. INTRODUCTION & LITERATURE REVIEW	1
1.1 Introduction.....	1
1.2 Research Objectives.....	2
1.3 Literature Review	4
1.3.1 Variable Mach-Number Wind Tunnels	4
1.3.2 Parameter Control	5
1.3.3 Flow Quality Characterization and Uncertainty Quantification	7
1.3.4 Hysteresis in Hypersonic Flows	8
2. DESIGN AND FABRICATION OF ACE2.0	9
2.1 Background and Motivation	9
2.1.1 ACE Turbulent Transition.....	9
2.2 ACE2.0 Design	15
2.2.1 Design Requirements.....	16
2.2.2 Nozzle Contour Codes	19
2.2.3 CFD	20
2.2.4 General Nozzle and Settling Chamber Design	21
2.2.5 Mechanical Design Iterations	22
2.2.6 20-Ton Linear Actuators Design	25
2.2.6.1 Nozzle and Settling Chamber Design	26
2.2.6.2 Frame Design	27
2.2.6.3 Actuation System Design	27
2.2.6.4 Final Overall Design	31
2.2.6.5 FEA	31
2.3 Fabrication Plans	31
2.3.1 Pressure Test	35
2.3.2 Polishing	35
2.4 Final Assembly, Installation, and Calibration.....	35
2.4.0.1 Nozzle Alignment	36

2.4.1	Actuation Homing and Calibration	36
2.4.2	Shakedown and First Runs	37
3.	EXPERIMENTAL APPROACH & OBJECTIVES	38
3.1	Improved Experimental Control and Efficiency	38
3.1.1	Feedback-Controlled Active Mach Number Variation and Selection	38
3.1.2	Reynolds Number Control Scheme	40
3.2	Freestream Flow Uniformity and Disturbance Levels Characterization	43
3.2.1	Freestream Uncertainty Quantification	44
3.2.2	Freestream Disturbance Hysteresis	47
3.3	Mach Trajectory and Potential Hysteresis Proof of Concept Experiment	47
4.	REAMAINING WORK	55
4.1	Maybe.....	55
4.2	Possibly	55
	REFERENCES	56
	APPENDIX A. ACE2.0 NOZZLE CONTOUR.....	62
	APPENDIX B. CFD RESULTS	64
	APPENDIX C. ACTUATION SPECIFICATIONS	65
C.1	Detailed Parts Lists and Decritptions	65
C.2	Mach Number Control Program.....	65
	APPENDIX D. TUNNEL INFRASTRUCTURE	66
	APPENDIX E. OPERATING PROCEDURES	67
	APPENDIX F. DETAILED FABRICATION DETAILS	68

LIST OF FIGURES

FIGURE	Page
1.1 ACE tunnel schematic	5
2.1 ACE nozzle and settling chamber	9
2.2 ACE throat discontinuity	10
2.3 ACE freestream pressure fluctuations in the nozzle exit plane as measured in 2014 ..	12
2.4 ACE freestream pressure fluctuations at various locations as measured ii 2019	13
2.5 ACE freestream pressure fluctuations at 6 inches and 17 inches upstream of nozzle exit as measured in 2022	14
2.6 Sidewall mushroom vortex formation (upper quadrant/quarter) at 24 inches upstream of nozzle exit (top) and at nozzle exit (bottom)	15
2.7 Görtler number from ACE nozzle CFD	16
2.8 N-factors for Görtler number in ACE nozzle	17
2.9 Mach lines for noise measured at 17" upstream on nozzle exit.	18
2.10 Comparison of ACE (quadratic) and ACE2.0 (quartic) expansion at throat	20
2.11 Mesh in Pointwise for ACE (top) and ACE2.0 (bottom) nozzle contours.....	21
2.12 ACE2.0 CFD Mach number plot	21
2.13 Comparison of ACE (top) and ACE2.0 (bottom) nozzle and settling chamber designs	22
2.14 Iteration 1 of ACE2.0: Non-active	24
2.15 Iteration 2 of ACE2.0: Sliding Wedge	24
2.16 Iteration 3 of ACE2.0: Rollers and Actuators	25
2.17 ACE2.0 final nozzle and settling chamber with actuators.	26
2.18 CAD of frame	28
2.19 CAD model of 20-ton linear actuator, 20:1 gear box, and servo motor.	29

2.20	Inverted disc springs stacks at the end of the settling chamber.....	30
2.21	Full CAD model of ACE2.0 in Solidworks	32
2.22	Side view of ACE2.0 in Solidworks.....	33
2.23	Manufacturing schedule beginning from September 25, 2023.....	34
2.24	Rough cut brace on water jet.....	34
2.25	Planned water jet layout for frame parts.....	35
2.26	Pallet of finished frame parts from FEDC.....	36
2.27	Nozzle block saw cut to rough profile.....	37
2.28	Nozzle assembly for shipping to polishing vendor.	37
3.1	ACE freestream pressure fluctuations.....	44
3.2	Pitot probe measuring 24 inches upstream of nozzle exit.	45
3.3	Flow over wedge resulting in regular reflection of shock	50
3.4	Flow over wedge resulting in Mach reflection of shock.....	51
3.5	Double wedge setup.....	52
3.6	Shock wave reflection configuration domains for Mach number and wedge angle.	53
3.7	Mach-number-varitation-induced hysteresis for 27° wedge	54
A.1	A caption here	63
B.1	A caption here	64
C.1	A caption here	65
D.1	A caption here	66
E.1	A caption here	67
F.1	A caption here	68

LIST OF TABLES

TABLE	Page
3.1 Test matrix for ACE2.0 freestream characterization.....	46

1. INTRODUCTION & LITERATURE REVIEW

1.1 Introduction

In recent decades, the continual improvement in hypersonic aerodynamics has emphasized the need for advancements in wind tunnel ground testing capabilities [1]. Conventional hypersonic wind tunnels rely on distinct fixed nozzle contours to accelerate the flow to the desired Mach number. This approach fixes the Mach number so it only provides a particular flow regime for experiments. Recognizing this, there is a clear need for a continuously variable Mach-number nozzle designed to overcome the limitations of conventional wind tunnels and enable more advanced dynamic hypersonic research.

The objective of this work is to introduce a continuously variable and actively controllable Mach-number nozzle. By dynamically adjusting the throat height and thereby the Mach number throughout the wind tunnel runs, the variable conditions experienced by hypersonic vehicles during different flight trajectories can be effectively modeled. This capability would enable the advancement of ground testing for a more comprehensive understanding of dynamic hypersonic flight and associated phenomena. Furthermore, the active control capability will increase experimental efficiency by allowing measurements at different Mach numbers within a single run and introduce the ability to fine tune the Mach number for improved data quality. However, this variable Mach number capability does introduce the challenge of maintaining desired Reynolds numbers, so feedback control will also be explored for the Reynolds number to counteract this and improve the overall experimental control.

The Actively Controlled Expansion (ACE) wind tunnel at Texas A&M University has served as a workhorse in hypersonic research since 2010 [2–8], and is due for improvements to meet the growing demand of hypersonics research. Although the facility was initially designed to facilitate the continuous variation of Mach number, the mechanical implementation ultimately proved to be cumbersome to adjust. Consequently, the nozzle has remained fixed at Mach 6 for the majority

of the tunnel's operation, falling short of fully realizing its designated variable Mach capability. Additionally, despite the geometry being fixed, the Mach number actually varies throughout a run by up to 5%. Considering this, it is apparent that an update to the ACE nozzle is necessary to remedy these shortcomings.

1.2 Research Objectives

The objectives of this research aim to lay the foundation for continuously variable and actively controlled Mach number capabilities at the National Aerothermochemistry and Hypersonics Laboratory (NAHL). Doing so will expand the current capabilities within the lab for more advanced hypersonic aerodynamics experiments. This will help maintain the NAHL as a cutting-edge national research facility. The existing ACE facility will be upgraded to achieve true active control and to potentially produce low-disturbance flow for higher Reynolds numbers. Its successor, ACE2.0, that is the subject of this work, will employ a feedback-control system with servo motors, linear actuators, and various instrumentation to enable the accurate and continuous variation of Mach number by changing the throat height. Additionally, active feedback-control of the Reynolds number will be developed and potentially implemented.

Once fabricated and calibrated, the ACE2.0 facility will provide:

1. Improved experimental control and efficiency

An active throat height control system will be implemented to enable active feedback-controlled Mach number variation and selection for Mach trajectories and accurate set points. The feedback aspect will attempt to control the Mach number to within 0.5% of the set value. An active control scheme will also be developed to enable feedback-controlled Reynolds number variation and selection that responds to changes in Mach number and stagnation temperature for accurate sweeps and set points. This will allow both constant or varying Reynolds number during a Mach trajectory. The Reynolds number controller will be fully designed but may not be implemented due to constraints.

The control of both of these parameters will yield improved experimental efficiency with

a new capability to explore multiple flow configurations within a single run. Besides enhancing efficiency, the Mach number and Reynolds number control will enable more robust uncertainty quantification and more dynamic experiments that were not possible before. Both of these capabilities are demonstrated in the next objectives.

2. Characterization of freestream flow uniformity and disturbance levels throughout the nozzle and uncertainty quantification of flow parameters

A flow survey of the nozzle exit plane and centerline will be conducted to measure the freestream flow uniformity and disturbance levels throughout the nozzle and characterize its performance. This will validate the design and manufacturing of the nozzle and settling chamber and provide a basis for the quality of data gathered in future experiments. A rigorous uncertainty analysis will be performed to quantify the systematic and random uncertainty of the measured flow parameters P , P_0 , and T_0 and the resulting values of Mach number, M , and unit Reynolds number, Re' . This will establish the baseline uncertainty for the freestream flow parameters and enable improved data quality for future experiments. In order to fully characterize the tunnel behavior while actively controlled, an investigation of the potential existence of hysteresis phenomena will be performed. If discovered, any hysteresis will be characterized to fully understand the dynamics of the freestream flow as each parameter is varied.

3. Demonstration of Mach trajectory operation and potential hysteresis in a proof of concept experiment

The capabilities of ACE2.0 will be demonstrated in an experiment that will showcase shock wave interactions between two wedges during a Mach trajectory. This experiment will explore a well-known hysteresis in the transition from a regular reflection to a mach reflection and the ability to produce the phenomenon in this facility.

These objectives will effectively validate and demonstrate the capabilities and merit of the new ACE2.0 facility. In addition, the standard operating procedures for ACE2.0 will be updated to

reflect the best practices deduced throughout the completion of these objectives. The resulting control procedures and interface will be straightforward and well documented so that future users can easily learn to effectively operate the facility. The documentation will not only enhance the accessibility of ACE2.0 for subsequent research endeavors but also contribute to the broader scientific community by providing a robust framework for effective wind tunnel control and dynamic hypersonic vehicle aerodynamics exploration.

1.3 Literature Review

The literature review for this dissertation includes four parts related to hypersonic variable Mach-number wind tunnels and according to the above objectives: (1) variable mach number nozzle design, (2) parameter control, (3) flow quality characterization and uncertainty quantification, and (4) hysteresis in hypersonic flows. This review will discuss articles that establish the most current knowledge base and techniques in the relevant areas of hypersonic wind tunnel research.

1.3.1 Variable Mach-Number Wind Tunnels

Variable Mach number nozzles have been explored in many configurations since the 1950s such as interchangeable fixed-block, plug-type, asymmetric sliding blocks, tilting plate, fully flexible, and hinged/flexure [9]. Each of these designs have varying degrees of flow quality, cost effectiveness, and experimental efficiency that must be considered. Only the fully flexible and flexure designs maximize experimental efficiency without sacrificing flow quality. Of these two, the flexure design minimizes costs by reducing mechanical complexity and supporting structure. Therefore, the flexure design is the optimal choice considering these criteria.

The flexure type nozzle was first proposed in 1955 by Rosen [10] and improved upon separately by Erdmann in 1971 [11] and Rom and Etsion in 1972 [11,12] in order to minimize the mechanical complexity. This simple nozzle design operated by a single jack greatly reduces manufacturing and controls costs and allows for greater flexibility in active control to quickly and continuously vary the Mach number to model dynamic supersonic vehicle flight.

In the last decade, many variable mach number supersonic wind tunnels have been manufac-

tured due to increased demand of hypersonic flight research. The majority of these are fully flexible or flexure nozzle designs with varying implementations of actuation and control [13–21]. All of these facilities were developed to study vehicle flight trajectory and the hysteresis phenomenon therein.

Duplicate at start of chapter 2? The ACE tunnel, the facility of interest for this work, has been in operation since 2010 [2–4]. The nozzle is a flexure type that produces Mach 5 to 8 flow in a 9 inch by 14 inch test section. The flexure design is effective in achieving the change in throat height, but it cannot be done continuously and actively during a run. This is the primary issue to be addressed in this work.

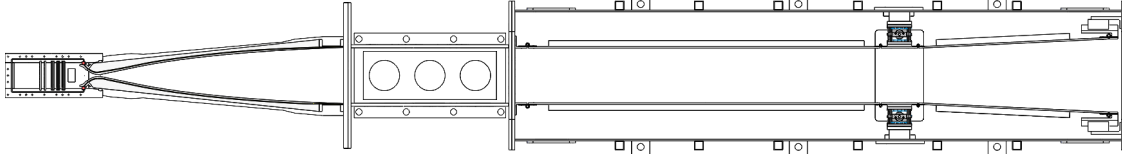


Figure 1.1: ACE tunnel schematic

1.3.2 Parameter Control

A variable Mach number facility requires effective control schemes for the controllable parameters A^* , P_0 , T_0 , and the resulting Mach number, M , and unit Reynolds number, Re' , in order to vary each parameter independently and accurately. This control problem, acknowledged as early as the 1980s, prompted the development of diverse solutions implementing the various areas of control theory such as optimal control [22, 23], state feedback control, mathematical model prediction control, preprogrammed controllers [24], and PID control [25–27].

In recent years, researchers at numerous variable Mach number facilities have embraced advanced intelligent control methods. Techniques such as fuzzy logic, genetic algorithms, neural networks, adaptive control or gain scheduling, and their combinations have been applied [14, 28]. The methods that will be explored in this research are those of Hwang et al. [23], Matsumoto et

al. [24], Ilić et al. [26], and Shahrababaki et al. [14] as they each introduce the different advantages and challenges of each control technique.

Hwang et al. [23] developed a robust LQG/LTR (Linear Quadratic Gaussian with Loop Transfer Recovery) controller enhanced by an anti-integrator windup and a modified Smith predictor to overcome unavoidable modeling errors, uncertainties, and time-delay effects. This controller demonstrated a faster stabilization and exhibited fewer oscillations in comparison to its PID counterpart. Given its superior performance, it presents an appealing prospect for implementation in ACE2.0, and a detailed exploration of this controller will be undertaken in a subsequent chapter.

Matsumoto et al. [24] took a simplified approach by replacing an existing real-time PID controller with a preprogrammed controller to avoid input time delays. This was advantageous for the facility used in that work because the run time was not much longer than the time delay for the PID controller to stabilize. This is the most straightforward approach to obtain specific constant or dynamic trajectories of multiple input parameters but it has limitations. The controller must have a new program for each individual desired parameter set condition or path, and each program must be iterated to minimize errors. Considering these limitations, a preprogrammed controller will be a backup option that will only be explored if necessary. Considering the longer run times of ACE2.0, a PID controller can be implemented with ample time to stabilize.

Ilić et al. [26] implemented a cascade nonlinear feedforward-feedback PID controller as a combined system to enhance a standard single-loop PID. The system's set point reference tracking is improved by the feedforward-feedback architecture, and the disturbance rejection is improved by the cascade architecture. With these two architectures combined in one multi-loop controller, large transient overshoots are eliminated, set point settling times are decreased, and the overall accuracy of the controlled parameters is maximized. Once again, the improved performance of this controller makes it another appealing prospect for ACE2.0, which will be discussed later.

Shahrababaki et al. [14] utilized an artificial neural network and fuzzy logic to enhance a conventional PD controller to handle the complex nonlinearity of the variable mach number wind tunnel flow parameters. The advantages of fuzzy logic include its simplicity and adaptability of

introducing new control rules to handle imprecise data, uncertainty, and unmodeled dynamics. The combined advantage that Shahrabaki et al. explores pertains to the utilization of the neural network to develop the membership functions for the fuzzy logic controller. They designed and trained a feed-forward multilayer perceptron neural network according to the database from the mathematical model of the wind tunnel behavior in order to develop the optimal membership functions. This method will only be explored further for ACE2.0 if the methods of Hwang et al. or Ilić et al. do not yield sufficient performance.

1.3.3 Flow Quality Characterization and Uncertainty Quantification

The primary references regarding flow quality characterization will be the recent AIAA articles by Chou et al. [29] and Duan et al. [30] on hypersonic wind tunnel freestream disturbance measurements. These provide the latest measurement processes and procedures and reference over 50 publications on relevant topics from recent decades. In addition to these two references, a decade of NAHL experience and best practices will guide the characterization of ACE2.0 upon its fabrication and initial shakedown. Key NAHL ACE references on the freestream characterization of ACE are the AIAA paper by Semper et al. [5] and multiple dissertations by Mai [6], Neel [7], and Leidy [8]. Additionally, Leidy performed an uncertainty analysis in the existing ACE tunnel that will provide a rough baseline reference for the uncertainty quantification for ACE2.0.

The primary references for the uncertainty quantification in this research will be the NASA report by Stephens et al. [31], the forthcoming AIAA Guide on Uncertainty Quantification [?], and the dissertation by Curriston [32]. The methodology in this NASA report combines the techniques of the prevalent literature on the subject from the last few decades to quantify the uncertainty of the flow parameters in a supersonic wind tunnel. Curriston's work provides a secondary reference as he thoroughly demonstrates this methodology and that of the forthcoming AIAA guide as a case study in a low speed wind tunnel. The approach described in these references includes a sophisticated treatment of systematic uncertainty using a Mont Carlo method combined with direct comparison of replicate data to characterize random error. Curriston [32] also extensively treats pre-test and real-time uncertainly quantification to enhance test campaign quality control and decision support.

1.3.4 Hysteresis in Hypersonic Flows

A review of the literature on hypersonic flow hysteresis yielded many publications discussing shock interactions and inlet start/unstart processes. The inlet start/unstart literature will not be referenced directly in this work but will be valuable for future research in ACE2.0. Focusing on the shock interactions, Hornung et al. [33] first predicted hysteresis in the transition from regular reflection to Mach reflection, but they were unable to experimentally produce the hysteresis effect [34]. Recent literature reveals numerical investigations easily reproduce shock interaction hysteresis [35, 36], while experimental investigations prove more difficult due to the freestream noise in conventional facilities [16, 37]. The two processes that produce hysteresis in the shock interactions are wedge-angle variation and Mach-number variation [38]. Since it is significantly more complex to vary the Mach number, most experimental results are found by the wedge-angle-variation-induced hysteresis in open-jet, low-noise wind tunnels [39–44]. Some research groups with variable Mach number tunnels have attempted to reproduce shock interaction hysteresis experimentally by varying the Mach number, but they have all been unsuccessful due to the presence of high freestream disturbance levels [15, 45]. Methodologies from the numerical and experimental literature on Mach-number-variation-induced hysteresis will be studied in order to attempt to reproduce shock interaction hysteresis in ACE2.0.

2. DESIGN AND FABRICATION OF ACE2.0

2.1 Background and Motivation

Should this paragraph be here or in lit review or both? The existing ACE tunnel was designed and manufactured between 2009 and 2010 and began operating in 2010 [2–4]. The nozzle is 40 inches long from the throat to the test section entrance. The test section is 14 inches wide and 9 inches tall. The last 4 inches of the nozzle is a thin flexure portion that allows the throat height to be varied from approximately 0.04 to 0.36 inches, which enables the test-section Mach number to be varied from Mach 5 to 8.

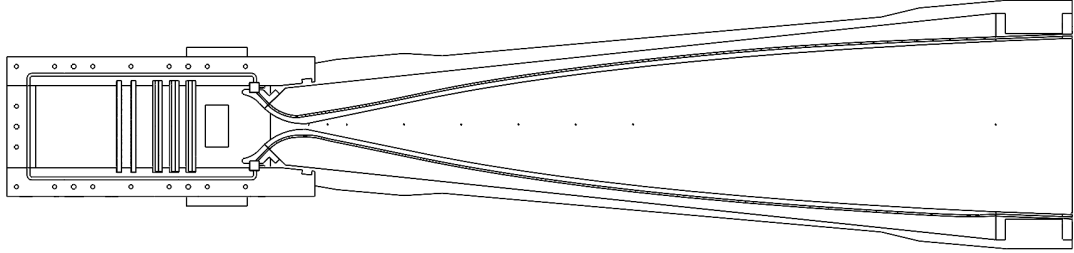


Figure 2.1: ACE nozzle and settling chamber

The original motivation for the redesign was to remanufacture the nozzle to remedy the premature laminar-to-turbulent transition, which is discussed in the next section. However, as the redesign progressed, it became apparent that this was the best opportunity to completely redesign the nozzle and settling chamber to enable active control. This progression and the redesign process is detailed throughout this chapter.

2.1.1 ACE Turbulent Transition

ACE performance data [5–8] shows that below a unit Reynolds number of $Re' = \frac{\rho U}{\mu} \approx 3 \times 10^6 / m$ the RMS pressure fluctuations in the test section are less than 1%, and that above this unit Reynolds number the pressure fluctuation levels significantly increase. It was desired to increase

the unit Reynolds number at which laminar flow can be maintained, so the mechanism causing laminar-to-turbulent transition of the nozzle boundary layers had to be determined. The hypothesis and supporting data regarding the pressure fluctuation levels increase and how it might be delayed to higher unit Reynolds numbers is summarized below.

Five primary suspects for transition were identified:

1. A known manufacturing surface discontinuity at the nozzle throat
2. Sidewall mushroom vortices
3. Görtler vortices
4. Freestream turbulence in the incoming flow and/or upstream boundary layer
5. Wall roughness or waviness

The throat discontinuity (1) is the result of a decimal truncation error when connecting the subsonic curve to the supersonic MOC contour in Solidworks. The resulting discontinuity can be seen in Figure 2.2, and it has a height of around 0.0003 inches. The artifact carried forward through the CNC machining and is present on the physical nozzle throat.

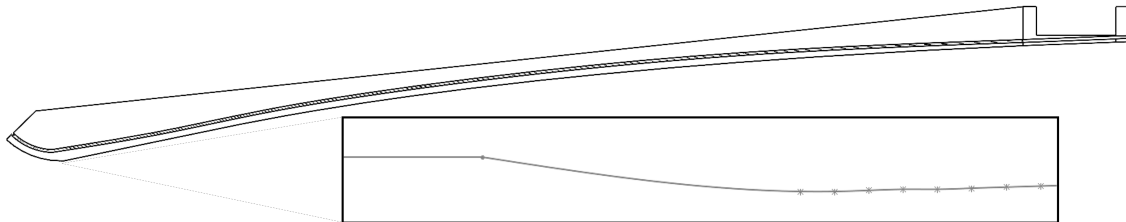


Figure 2.2: ACE throat discontinuity

The sections below evaluate each of these possibilities and support the conclusion that the throat discontinuity is the most likely reason for the increased pressure fluctuations above $Re' \approx$

3×10^6 /m. This conclusion is supported by pitot surveys, method-of-characteristics line tracing, and CFD simulations. Sidewall mushroom vortices (2) and Görtler vortices (3) would lead to transition too far downstream from the throat to be responsible for the pressure fluctuation levels increase. Incoming freestream turbulence (4) and wall surface quality (5) are potential causes of poor flow quality in all supersonic tunnels and are included for completeness. The specific mechanism by which these would cause transition is not known. While item 4 and 5 are not the primary suspects for the pressure fluctuation levels increase, improving these conditions will be addressed in the redesign intended to extend laminar flow to higher unit Reynolds numbers.

ACE Nozzle Noise Surveys

Three recent pitot surveys have been conducted in the ACE tunnel. The first by Mai in 2014 [6] revealed transition occurring around $Re' \approx 3 \times 10^6$ /m, as shown in Figure 2.3. The same result was found by Neel in 2019 [7] shown in Figure 2.4 that transition occurs at this Re' value at a location 6 inches upstream of the nozzle exit. A final pitot survey in ACE by Wirth in 2022 (unpublished) was conducted to determine whether the pressure fluctuation levels increase occurred at different Re' values at positions farther upstream in the nozzle. He found pressure fluctuation levels increase at $Re' \approx 3 \times 10^6$ /m at a measurement location 17 inches upstream of the nozzle exit. His results in Figure 2.5 align perfectly with Mai's and Neel's data and clearly establish that the Reynolds number at which pressure fluctuation levels increase is the same at all locations in the nozzle. This suggests that transition is not moving upstream through the nozzle as Reynolds number is increased.

Suspect Mechanism Conclusions

The pressure fluctuation levels revealed the Re' value at which transition occurs but not the transition mechanism. The two mechanisms that were extensively investigated at the start of this work were sidewall mushroom vortices and Görtler vortices. Sidewall mushroom vortices arise from the pressure distribution in the low momentum flow in the sidewall boundary layers. The flow at the centerline expands to the test section pressure ahead of the top and bottom curved walls.

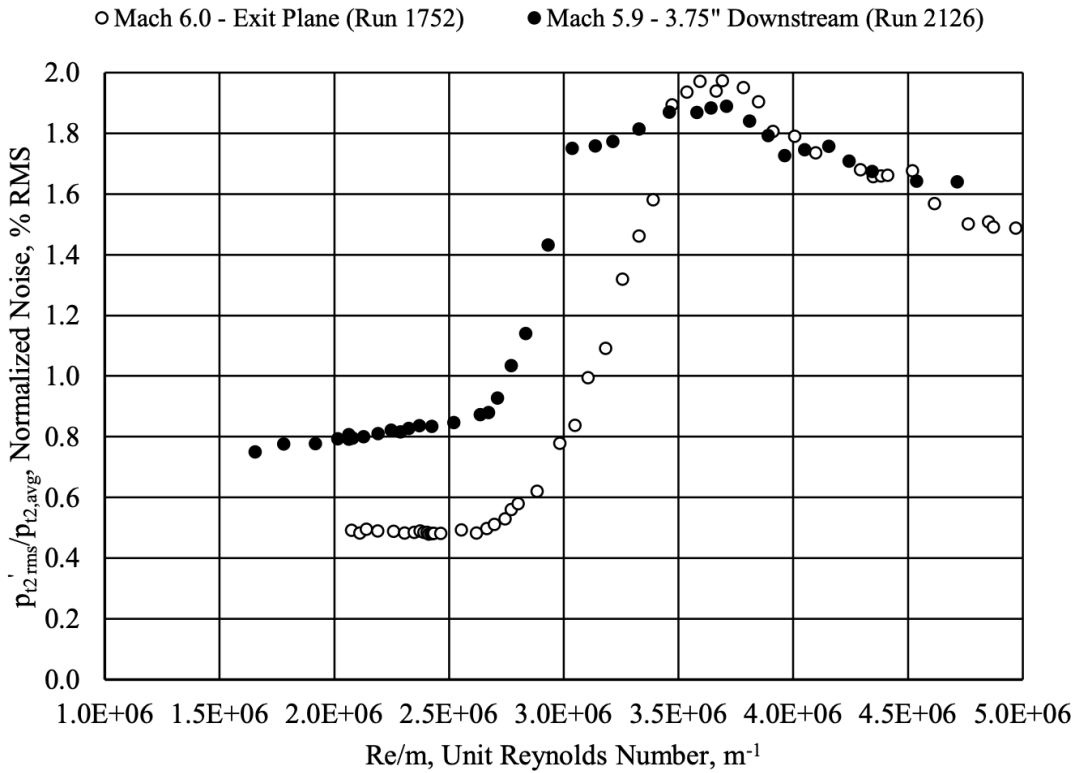


Figure 2.3: ACE freestream pressure fluctuations in the nozzle exit plane as measured in 2014 [6]

The flow at the top and bottom lags behind the centerline flow with a higher pressure to create a vertical pressure gradient that introduces a secondary vertical flow in the sidewall boundary layers that flows from the corners to the centerline [46]. CFD simulations by Kocian (unpublished) show the sidewall mushroom vortices beginning to form approximately 24 inches upstream of the nozzle exit shown in Figure 2.6.

Görtler vortices are counter-rotating streamwise vortices that occur in boundary layers on concave surfaces [47]. To estimate where these may lead to transition, a CFD basic state simulation and N-factor analysis was performed by Kocian in 2022 (unpublished). The results, shown in Figures 2.7 and 2.8, indicate that Görtler vortices could induce transition around 8 inches from the nozzle throat.

The origin of the noise measured farthest upstream of the nozzle exit was determined by tracing

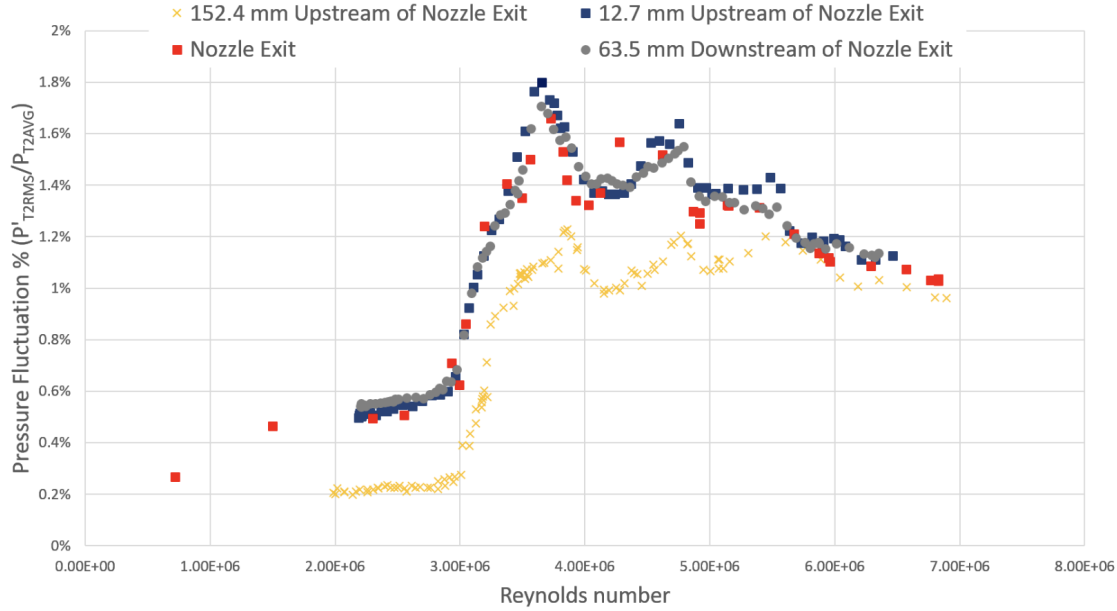


Figure 2.4: ACE freestream pressure fluctuations at various locations as measured in 2019 [7]

characteristic lines from the measurement location at the centerline upstream to the wall. Both the side view and top view of this can be seen in Figure 2.9. This was accomplished by choosing the characteristic output by the MOC code that intersects the centerline closest to the measurement point of 17 inches and tracing it back to its origin at the wall. The measured noise origin from the top view is upstream of the throat where sidewall mushroom vortices are not relevant, and the origin is near the end of the straight section of the nozzle where Görtler has not had sufficient time to induce transition. While both sidewall vortices and Görtler vortices can play some role in transition in planar nozzles, they are no longer considered suspects for the pressure fluctuation levels increase at unit Reynolds numbers above $3 \times 10^6 / \text{m}$.

Following the above conclusions and recommendations, the most likely reason the pressure fluctuations increase is laminar-to-turbulent transition due to a surface discontinuity at the throat. This conclusion is supported by pitot surveys, CFD, and method of characteristics line tracing described above. The remaining suspect mechanisms are still important to note and address in the redesign of the ACE tunnel.

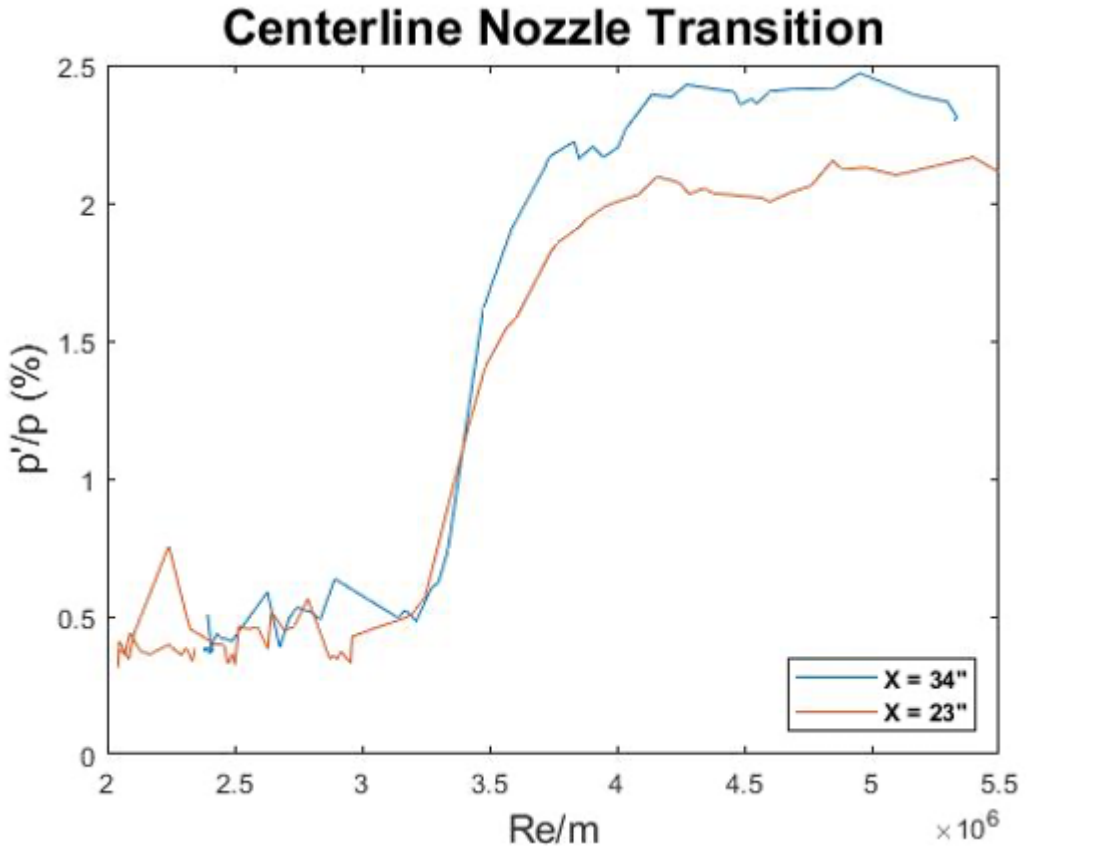


Figure 2.5: ACE freestream pressure fluctuations at 6 inches and 17 inches upstream of nozzle exit as measured in 2022

Design Recommendations

The following improvements are recommended to maintain laminar flow above $Re' \approx 3 \times 10^6/\text{m}$:

1. Second-derivative-smooth subsonic-to-supersonic throat transition to eliminate nozzle throat discontinuity
2. Continuous curvature with analytical functions to eliminate waviness and surface discontinuities
3. Enhanced surface polishing to minimize surface roughness
4. Improved settling chamber design to maximize flow uniformity and minimize freestream

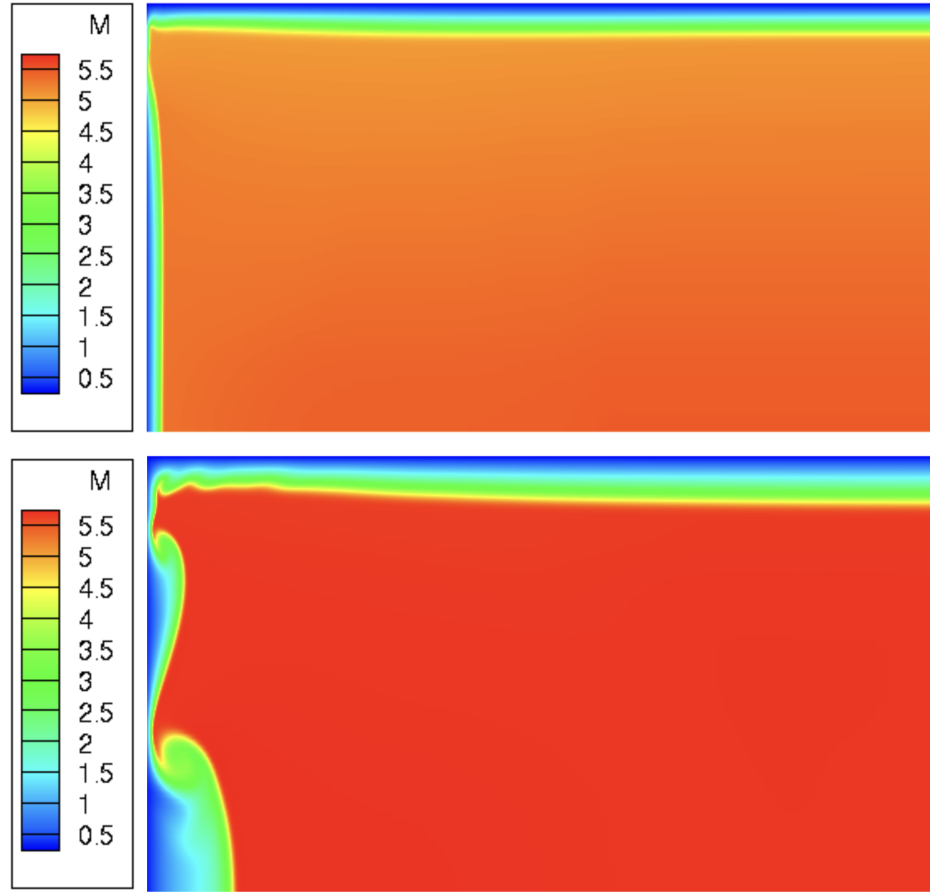


Figure 2.6: Sidewall mushroom vortex formation (upper quadrant/quarter) at 24 inches upstream of nozzle exit (top) and at nozzle exit (bottom)

turbulence upstream of the nozzle throat

One recommendation that is outside the scope of this work is to incorporate subsonic boundary layer suction to greatly reduce the incoming noise and potentially make ACE2.0 a "quiet" facility. Boundary layer suction is quite complex to effectively implement, but it will be accommodated for in the design in case it is explored in the future.

2.2 ACE2.0 Design

Following these recommendations, the nozzle will be redesigned and remanufactured to meet specific requirements that will ensure the best performance and potentially expand the laminar Reynolds number range. The decision to remanufacture the nozzle presents an opportunity to

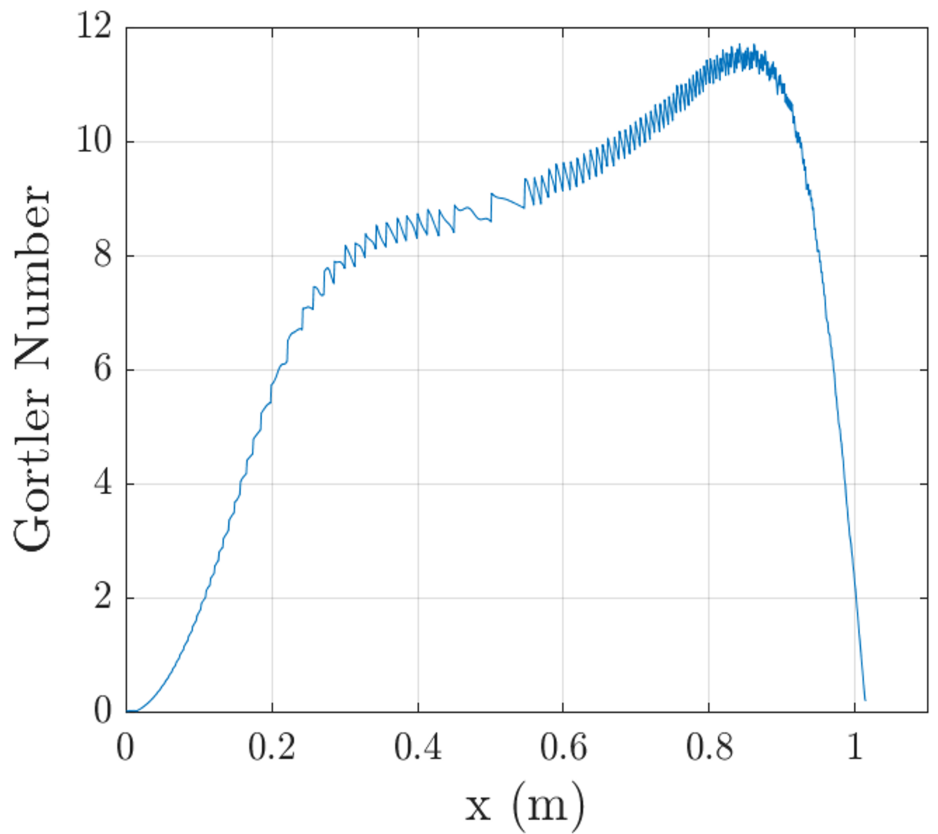


Figure 2.7: Görtler number from ACE nozzle CFD

revise the nozzle and settling chamber design to achieve true active controllability, properly embodying the "ACE" name.

The rest of the chapter details the planned improvements to the ACE tunnel and specific design requirements that will achieve those improvements. In addition to a new nozzle, the settling chamber will also be redesigned to ensure the uniformity and reduce the turbulence of the flow into the nozzle. These improvements are to achieve the goal of increasing the unit Reynolds number at which laminar nozzle flow is maintained.

2.2.1 Design Requirements

ACE2.0 will maintain many characteristics while improving some, so many requirements are the same as the original ACE design. The new tunnel will still produce uniform Mach 5 to 8 flow in the 9 inches by 14 inches test section, withstand a total temperature of 530 K, and maintain a

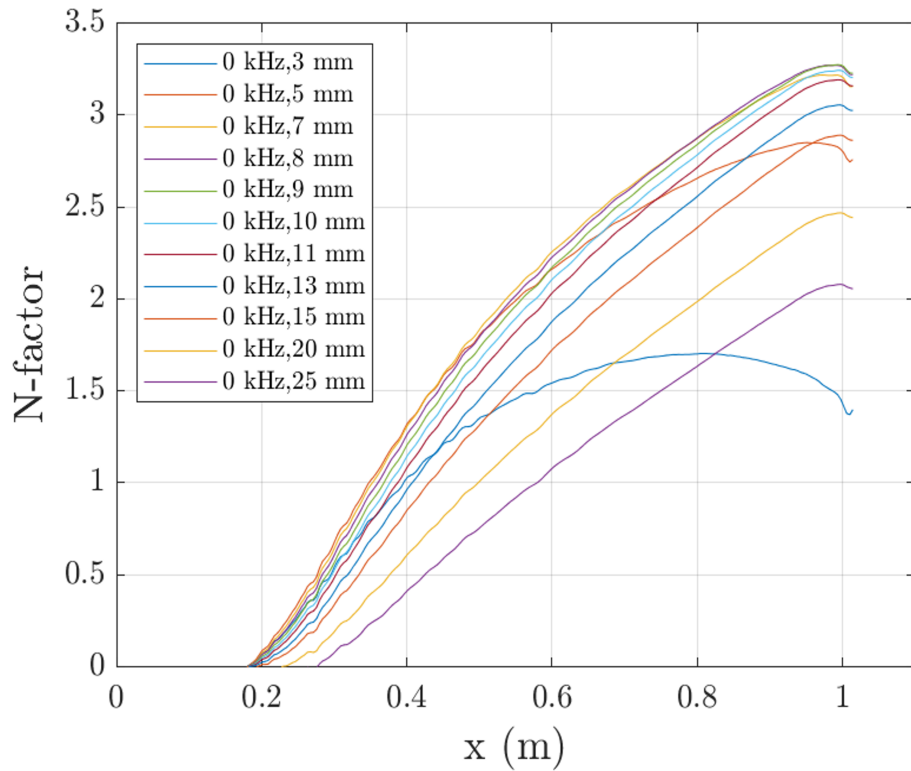


Figure 2.8: N-factors for Görtler number in ACE nozzle

minimum engineering factor of safety (FOS) of 1.5 when operating at a total pressure of 200 psia.

Nozzle Requirements

The current ACE nozzle successfully produces uniform Mach 5 to 8 flow in its core. In order to maintain this good performance and not introduce unknown parameters, the new nozzle will retain a very similar contour with slight improvements. The requirements that remain the same are that the nozzle must produce uniform flow for the entire Mach range, achieve maximum height deflection without exceeding a FOS of 1.5, and prevent leaks up to 200 psia.

The improvements to the nozzle and associated requirements will be a contour with continuous 1st and 2nd derivatives that is specified by analytical functions that will eliminate discontinuities and truncation error and a maximum allowable stress less than or equal to that found in the current ACE flexure at maximum deflection.

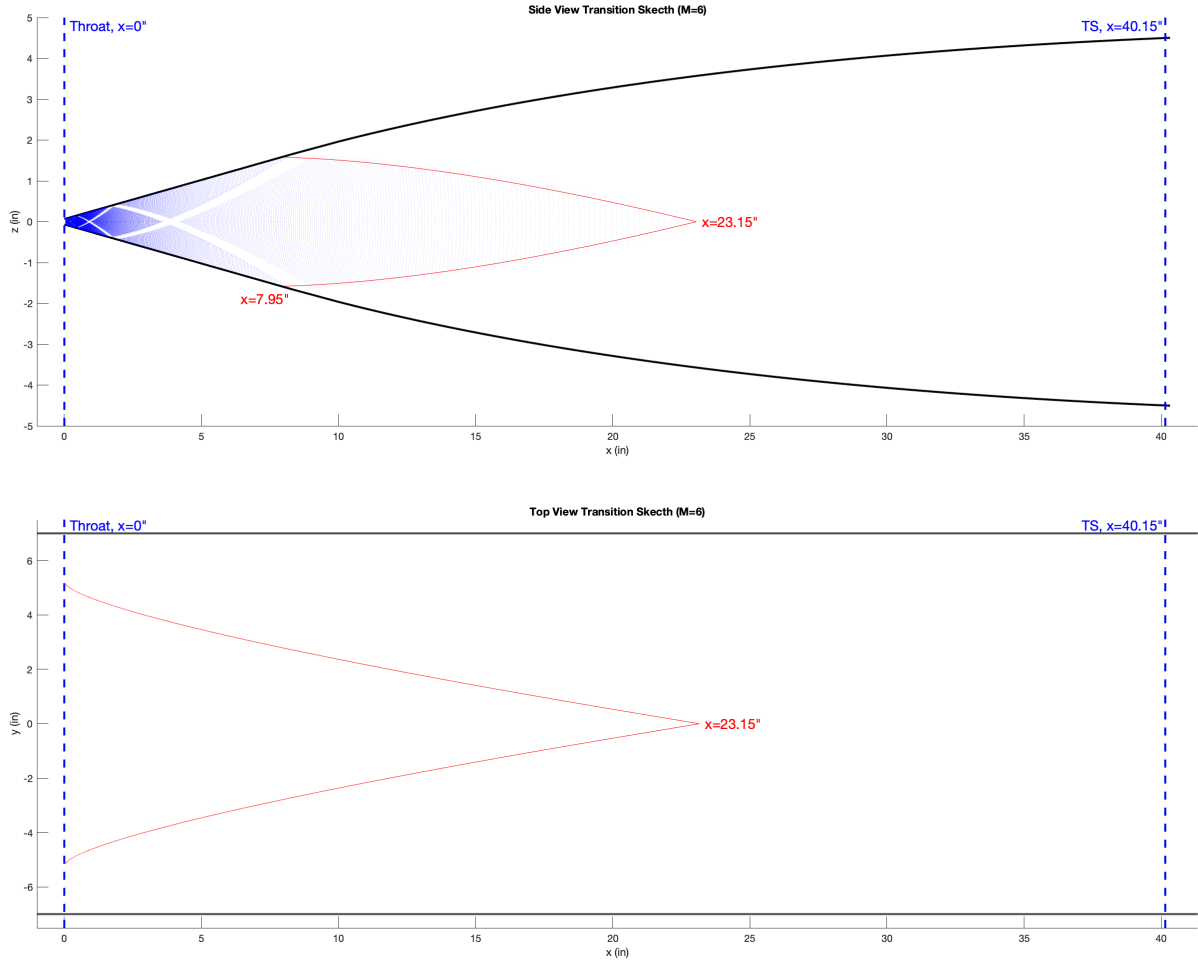


Figure 2.9: Mach lines for noise measured at 17" upstream on nozzle exit.

Settling Chamber Requirements

The current ACE settling chamber design provides multiple opportunities to improve flow conditioning and ease of maintenance. The new settling chamber design will increase the length and height and allow for variable aerogrid/screen configurations. The requirements that remain the same are low freestream turbulence, thin stable wall boundary layers, maximum uniformity, and preventing leaks at a pressure of 200 psia. The implementation of these requirements will be improved in the new design to achieve improved incoming flow into the nozzle.

Following Reshotko et al. [48], the length of the settling chamber shall accommodate a sep-

aration of 250 characteristic mesh sizes between screens allowing for adequate turbulence decay. The aerogrids will have a hexagonal perforation pattern to increase porosity and decrease pressure loss. The number of aerogrids and screens shall be variable to allow for future flow conditioning experiments. The inlet shall include a baffle system that will provide an acceptable initial distribution and mixing of the air received from the high-pressure inlet piping. The overall design will accommodate the option for future boundary layer suction slots.

A settling chamber height of 6 inches was chosen to keep the velocity as slow as possible without going below 10 ft/s for the majority of the Mach number range, according to Pope and Goin [49]. The reason for this minimum is to prevent thermal convection vortices from dominating the flow at the walls. The interior of ACE2.0 will also be heated prior to the start of the run to help avoid thermal gradients.

2.2.2 Nozzle Contour Codes

The multiple reflections method-of-characteristics (MOC) Fortran script written by Bowersox that produced the ACE nozzle contour was used for the new nozzle contour. In order to achieve continuous first and second derivative continuity, a section of the code was modified to produce a fourth-order expansion section instead of the original second-order curve. This allowed the expansion section to match the curvature of both the subsonic section and the straight section. The code modification is included in Appendix A, and a comparison of the original quadratic and the new quartic expansion sections is shown in Figure 2.10. In this figure, the ACE contour is directly from the MOC points and the ACE2.0 contour is specified by an analytic fourth-order polynomial. The waviness of the MOC points can be seen here, emphasizing the need to define the entire nozzle with analytic functions.

After the MOC points were produced by the Fortran script, they were imported into a MATLAB script to fit with analytic functions. The subsonic curve is given by a fifth-order polynomial with six boundary conditions of the settling chamber and throat heights and zero slope and curvature at both the start and throat. The straightening section is given by a function found using the `lsqcurvefit` function with a combination of power and logarithmic functions in MATLAB.

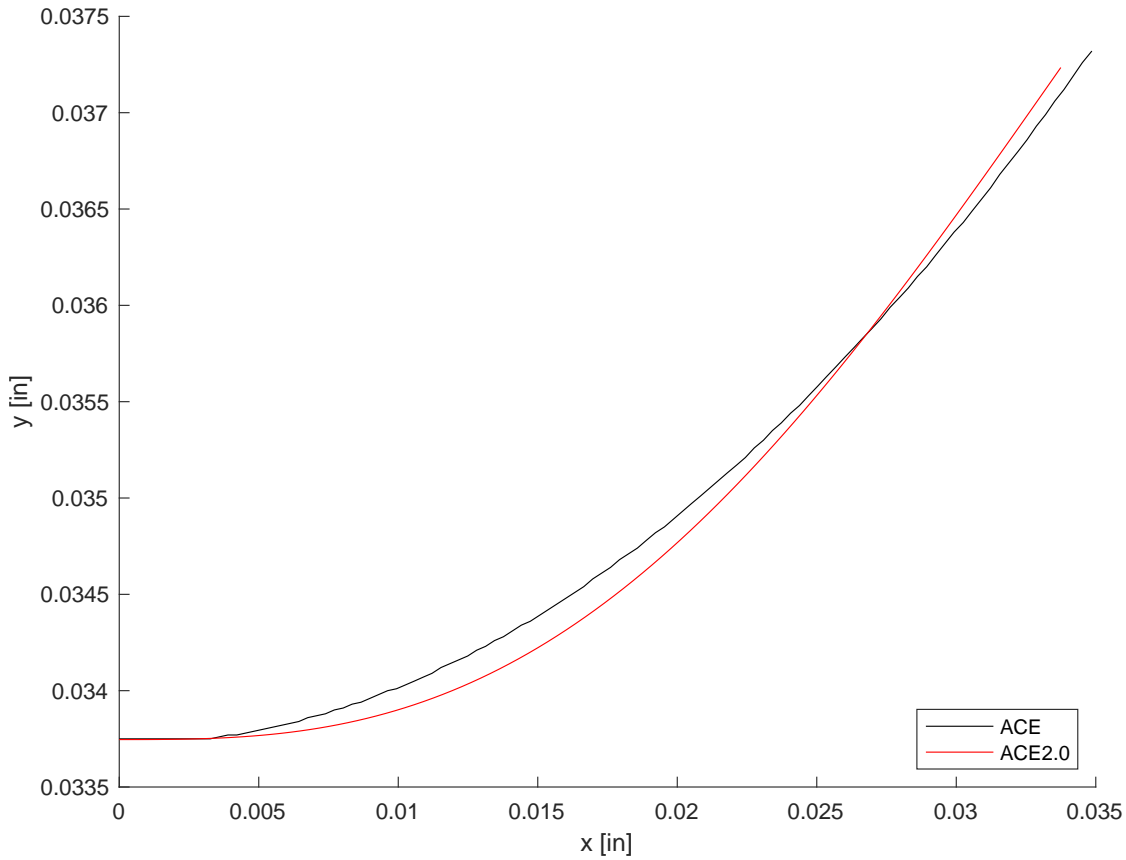


Figure 2.10: Comparison of ACE (quadratic) and ACE2.0 (quartic) expansion at throat

The equations for each section are given in Appendix A.

2.2.3 CFD

In order to verify the above nozzle contour performance compared to the original ACE contour, both contours were simulated in 2D CFD. First, a mesh was created in Pointwise for each contour with 400 equally spaced columns of cells in the x-direction. Each column had the spacing scaled to accurately capture the boundary layer with the smallest cell height around 4×10^{-6} inches at the curved wall and the largest around 0.2 inches at the centerline as seen in Figure 2.11. The CFD analysis was performed at a time when the settling chamber design was still at a height of 9 inches, so the analysis will be performed again to validate the 6 inch.

After creating a mesh for each, they were simulated using US3D on the Texas A&M supercom-

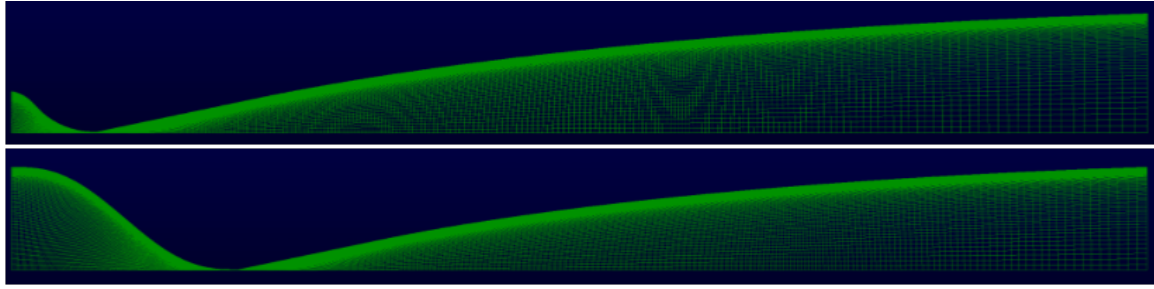


Figure 2.11: Mesh in Pointwise for ACE (top) and ACE2.0 (bottom) nozzle contours

puter, Grace. **Stuff about inputs and convergence conditions...** A sample of the results is shown in Figure 2.12. The full ACE2.0 CFD results compared to ACE is given in Appendix B.

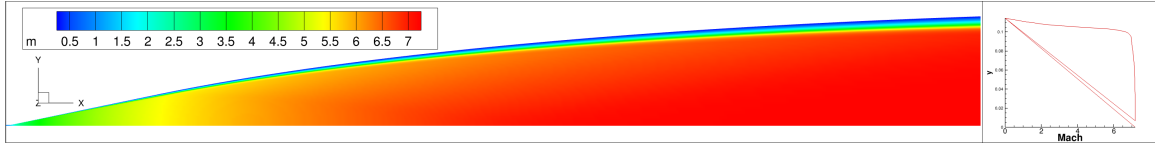


Figure 2.12: ACE2.0 CFD Mach number plot

2.2.4 General Nozzle and Settling Chamber Design

The resulting contour from above was imported into Solidworks using the analytic equations given in Appendix A, and the new ACE2.0 nozzle and settling chamber were designed following the above requirements. In order to accommodate the active control, the nozzle and settling chamber were combined into single rigid upper and lower pieces. Similar to ACE, the last 4 inches of the nozzle is a separate flexure piece to enable the variable Mach number capability. The overall length of the nozzle and settling chamber was increased by 19 inches with most of the added length contributed to the settling chamber.

The settling chamber is 1.7 inches taller and has a few considerable improvements. The flow conditioners are enclosed in a standalone box that allows for easy maintenance and future modifications of screen configurations. The initial configuration provides 3 inches between each aerogrid

and screen for adequate turbulence decay. Inlet flow spreaders are added as well to allow uniform mixing of the incoming air before flowing through the aerogrids.

The ACE design had the relative motion interface between nozzle and settling chamber with a large rubber seal that struggled to properly seal at higher Mach numbers. For ACE2.0, the end of the settling chamber is split into two pieces to allow the rotation of the nozzle blocks. This moves the potential sealing issue upstream of the flow conditioners where minor leaks are much less of a concern. The final ACE2.0 nozzle and settling chamber design compared to ACE is shown in Figure 2.13.

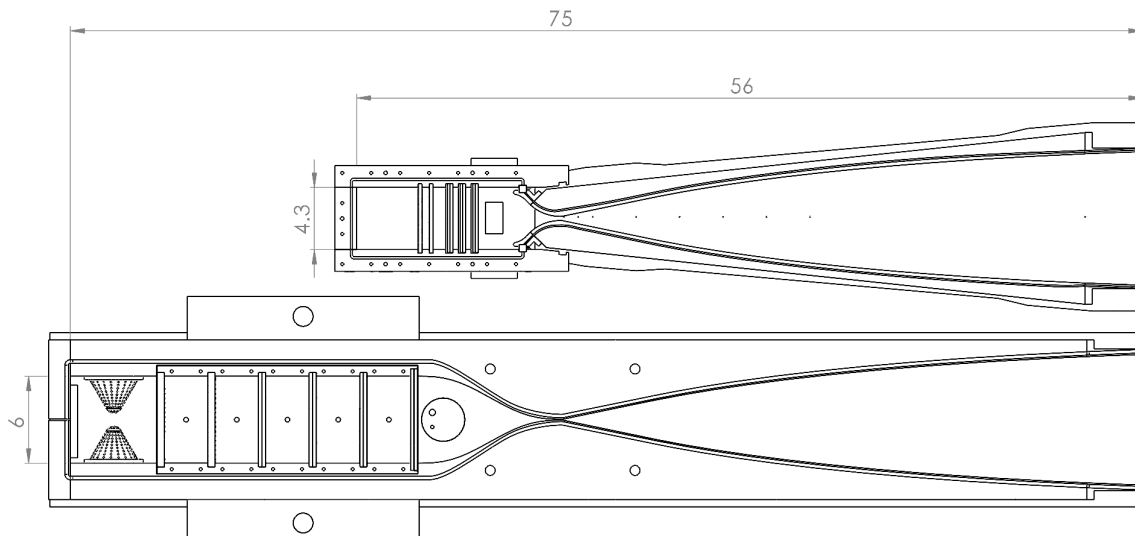


Figure 2.13: Comparison of ACE (top) and ACE2.0 (bottom) nozzle and settling chamber designs

All of the nozzle and settling chamber parts will be made from 304 stainless steel except for the flexures, which will be made from Condition A 17-4 PH stainless steel for maximum strength while maintaining flexibility.

2.2.5 Mechanical Design Iterations

There were a few distinct iterations throughout the design process of ACE2.0 that are worth mentioning briefly. As mentioned, enabling active control was not the original intent of the ACE

redesign, so the initial mechanical design was limited. One major difference to note between all of the past iterations and the final iteration is that the nozzle and settling chamber upper and lower pieces are not single rigid parts in the past iterations. The plan was to have either a bolted or welded interface between the nozzle blocks and the settling chamber piece to save cost in stock material, but it was decided to accept the higher cost of material for maximum strength and rigidity with a single piece.

A preface to the mechanical designs is that the actual load on the settling chamber and nozzle at a maximum pressure of 200 psia is around 90,000 pounds per top and bottom. This is the result of the increased surface area of the settling chamber and subsonic portion of the nozzle, which is 14 inches wide by 36 inches long.

The first iteration, shown in Figure 2.14, had a system of worm gears and lead screws to simultaneously adjust both nozzle blocks, and it required a jam nut on each lead screw and large wedges on the settling chamber to lock the position during a run. This design was not intended to be active, so it could not dynamically support the loads during a run. This design revealed that active control was not far from reach, so the next iteration began with the intention to enable it.

The second iteration, shown in Figure 2.15, built off from the idea of the wedges on the settling chamber to fully support against the loads during a run. This design relied on specially contoured oil-impregnated bronze sliding plates that were actuated by a similar system of worm gears and lead screws. The purpose of the contours instead of a simple flat wedge was to (1) provide a constant rate of change for the Mach number given a constant lead screw translation rate input and (2) maintain all points of contact as the nozzle rotated. The primary concern with this design was the expected wear and required actuation force due to friction, which would be around 20,000 pounds assuming a friction coefficient of 0.2 between the stainless steel and oil-impregnated bronze. This design also had the introduction of the disc spring stacks at the settling chamber end to hold the nozzles apart at the set position while not under load.

The third iteration, shown in Figure 2.16, improved upon the previous approach by introducing rollers and bearings to eliminate the friction and linear actuators for simpler and more robust

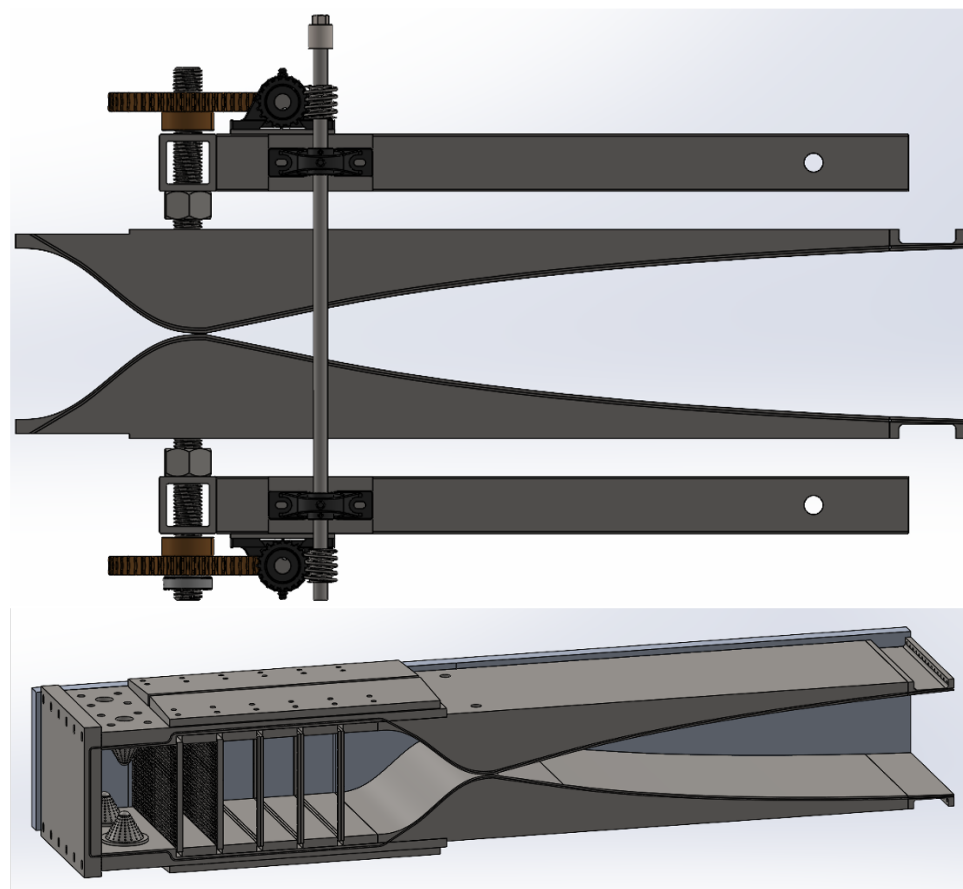


Figure 2.14: Iteration 1 of ACE2.0: Non-active

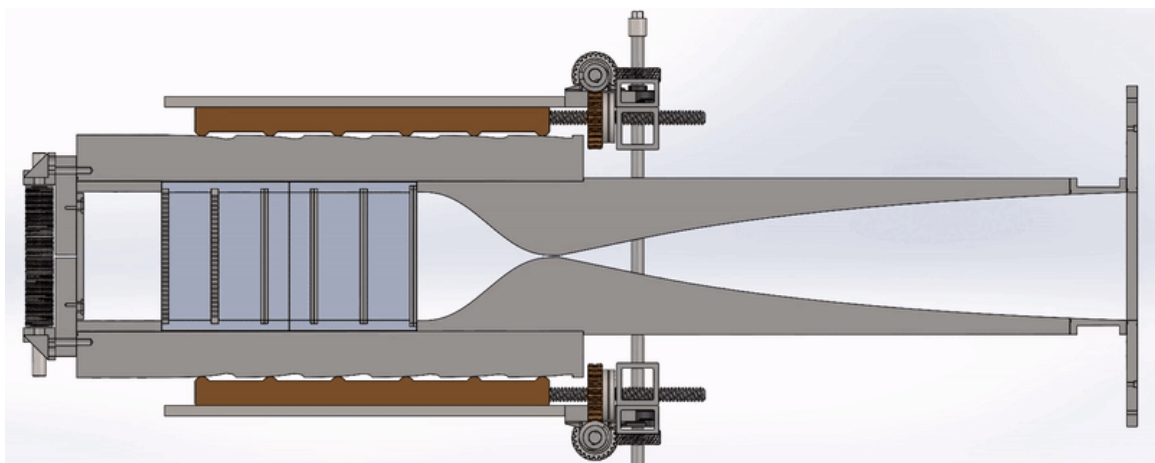


Figure 2.15: Iteration 2 of ACE2.0: Sliding Wedge

control. This design was abandoned for two primary reasons: (1) a realization that the reverse load while under full vacuum was unsupported and (2) feedback from machinists about concerns of wear in bearings and difficulty in machining the roller plate. The load under full vacuum across the entire nozzle and settling chamber is around 16,000 pounds, which requires substantial support to maintain the set Mach number when initiating a run and to minimize excess loads on the flexure.

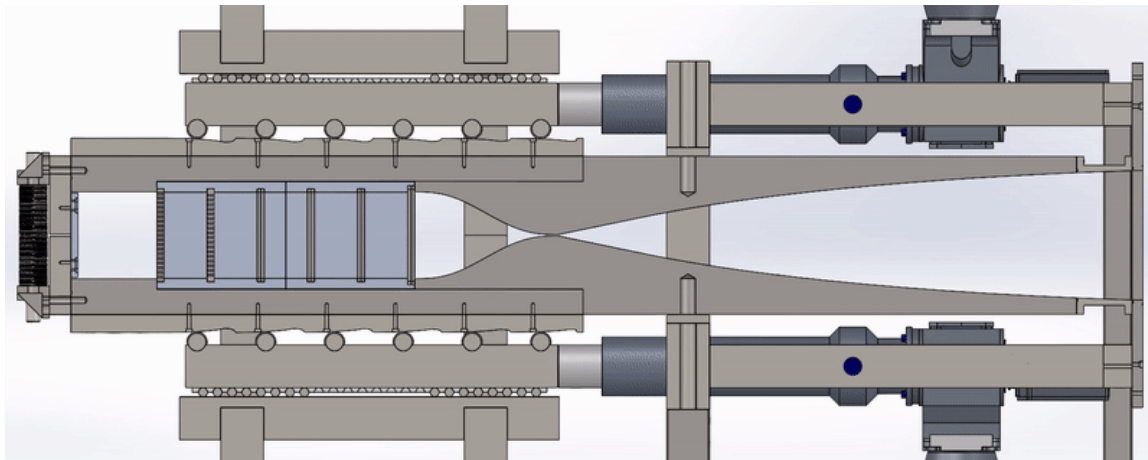


Figure 2.16: Iteration 3 of ACE2.0: Rollers and Actuators

The fourth and final iteration turned to a complete different approach of using 20-ton ball screw linear actuators to fully support both the maximum pressure and full vacuum loads. This final iteration is the most simple mechanically while also providing the most versatility in controlling the Mach number.

2.2.6 20-Ton Linear Actuators Design

The final design of ACE2.0 utilizes two 20-ton ball screw linear actuators on both the upper and lower nozzle blocks to actively control the Mach number by varying the throat height. The final design of the nozzle and settling chamber with the actuators can be seen in Figure 2.17.

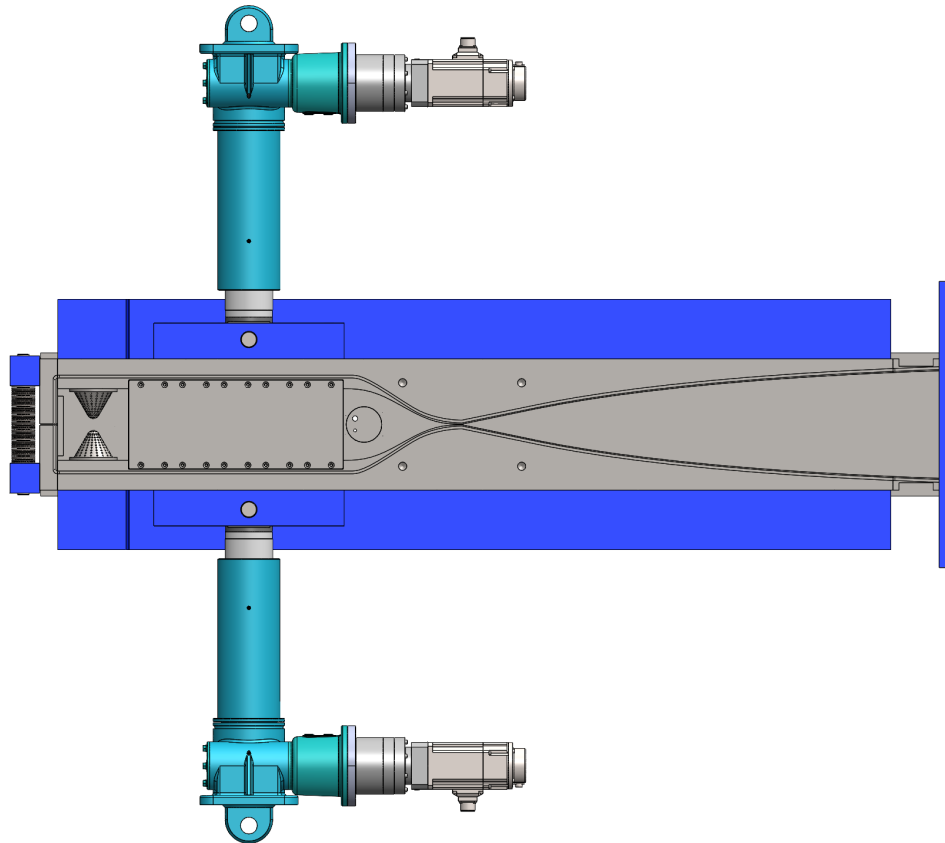


Figure 2.17: ACE2.0 final nozzle and settling chamber with actuators.

2.2.6.1 Nozzle and Settling Chamber Design

Using linear actuators does present the challenges of introducing stress concentrations at the attachment location and not providing support along the length of the nozzle and settling chamber. These were overcome by making the mating clevis on the settling chamber a 16 inch bar to distribute the load and adding a 5 inch by 2.5 inch beam along the length of the nozzle and settling chamber to provide rigidity, as seen in Figure 2.17.

The sidewalls are 1.5 inches thick and made from 304 stainless steel. They are handled and suspended from the frame by two brackets each, and a series of custom bar clamps will provide the support against the load under pressure. One sidewall has all of the ports and sensors, which allows the other to be the main access for maintenance. [Figure?](#)

The flow conditioner box is made from four 0.75 inch thick 304 stainless steel plates. This

assembly floats between the nozzles and is secured by the sidewalls in a slot. The overall height doubles as a safety limit so the nozzles will hit each side of the box before hitting each other. Housed inside the box is two aerogrids and four screens in the current configuration, but any configuration can easily be designed and swapped in the future. [Figure? And go into further detail on aerogrids and screens?](#)

2.2.6.2 *Frame Design*

The frame was designed around the linear actuators to best support the extreme loads. In order to maximize strength, a single piece brace was designed to symmetrically bear the loads from the actuators. The rest of the frame was designed between the brace and the nozzle-test-section flange to support the sidewalls. The entire frame will be made from 3 inch thick 4140 alloy steel plates and bars, and it all bolts together instead of welding. All exposed faces will be powder coated in order avoid rust and wear over time.

The frame will have four 5000-pound capacity steel swivel casters for easy maneuvering when aligning for installation. Once in position, the weight of the assembly will be transferred to rigid feet on threaded rods. All of these details can be seen in Figure 2.18.

2.2.6.3 *Actuation System Design*

The actuation system for ACE2.0 is comprised of many components that enable the active feedback-back control of the Mach number. Only a high level overview will be provided here for sake of brevity, but a full detailed description of the entire system will be provided in Appendix C.

The linear actuators are each rated for 40,000 pounds with a minimum FOS of 7. They have a double clevis design to rotate freely and have a custom motor mount for the selected gear box and servo motor, as shown in Figure 2.19. The actuators are comprised of a 24:1 worm gear reducer that turns a ball nut to drive a 0.5 inch lead ball screw. The ball nut has a long service life that will allow over 400,000 full throat deflections before maintenance is required. Another 20:1 gear box will be mounted to each actuator for an overall travel of approximately 0.001 inch per servo motor turn.

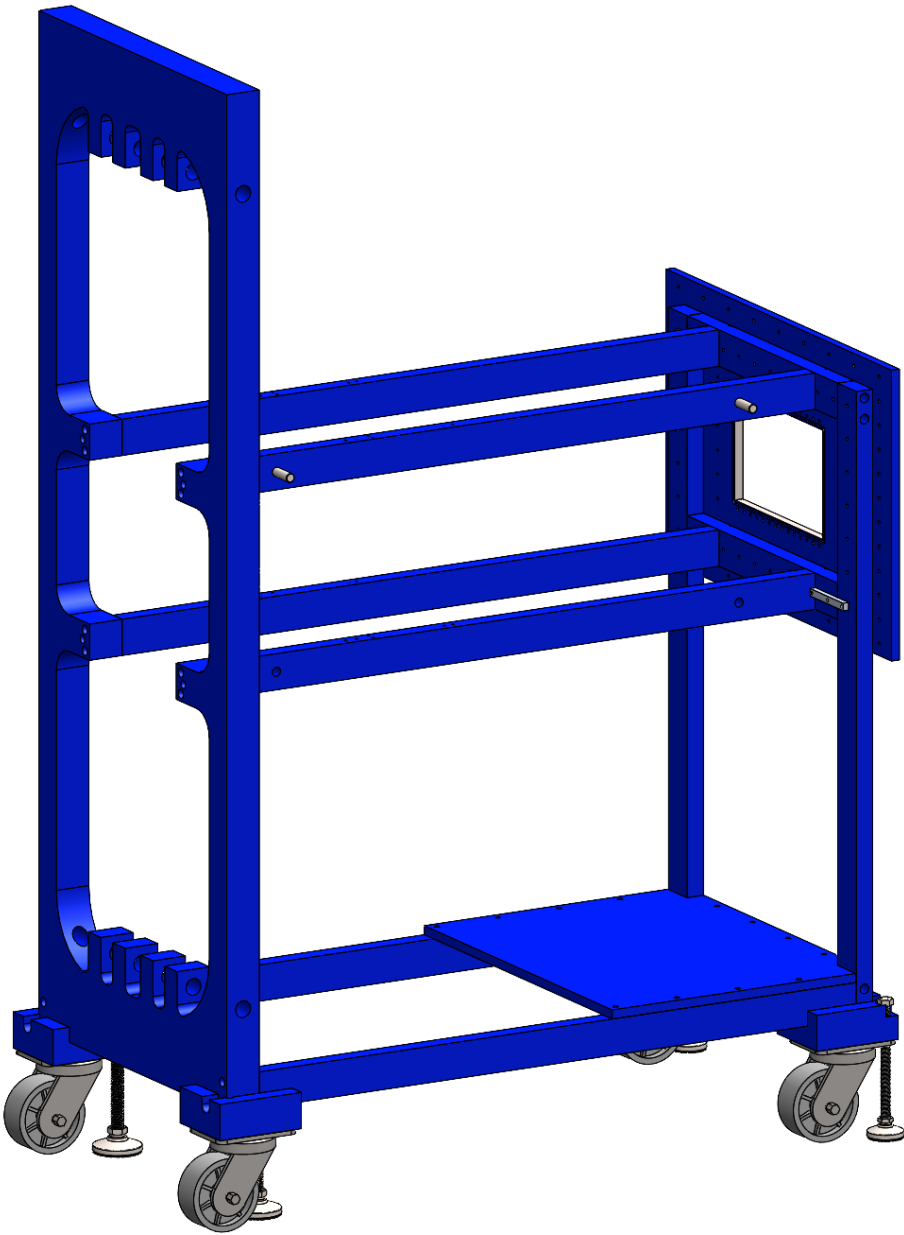


Figure 2.18: CAD of frame

The required input torque for the actuators at maximum load with the additional gearbox is 28 inch-pounds. The rated continuous torque and the momentary peak torque of the selected servo motor are 28 and 84 inch-pounds, respectively, and the rated continuous speed and the momentary peak speed are 3000 and 5000 revolutions per minute, respectively. The change in throat height from Mach 5 to 8 for each half of the nozzle is around 0.157 inches, so a full Mach sweep at

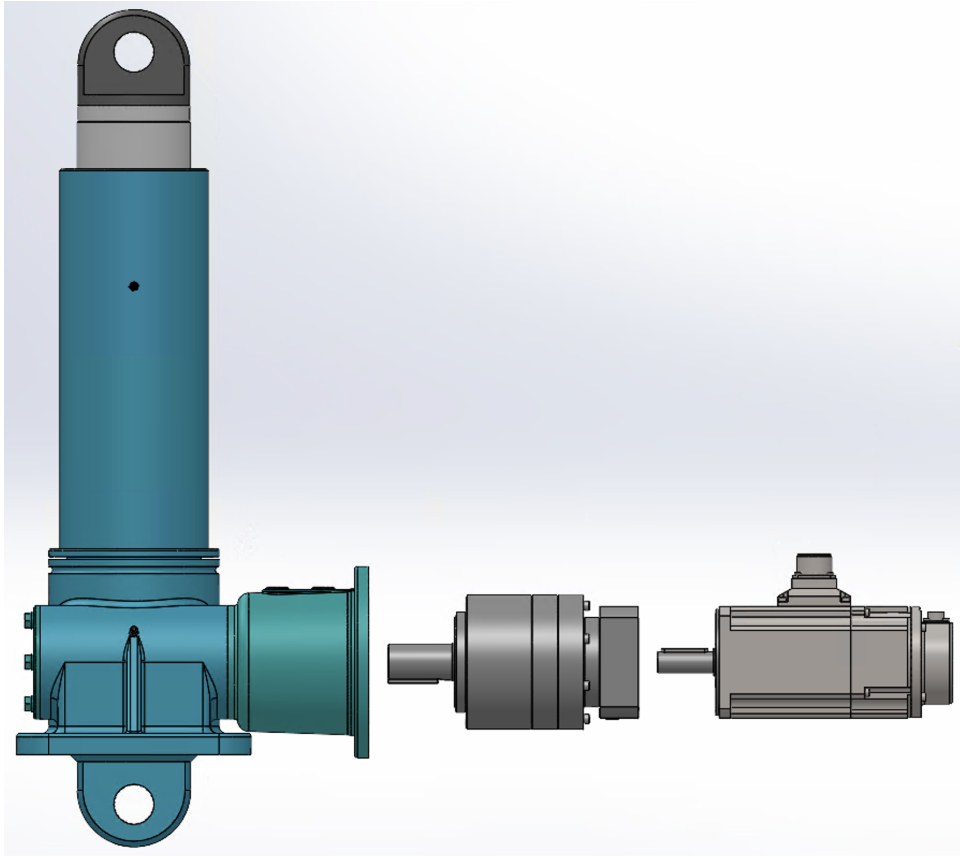


Figure 2.19: CAD model of 20-ton linear actuator, 20:1 gear box, and servo motor.

maximum pressure can be achieved in around 3 seconds within the continuous operation range of the servo motor. The servo motors have a power-off brake hold a set Mach number and to prevent motion and any potential damage in a power outage.

In order to minimize the backlash in the actuators, two inverted stacks of Belleville disc springs were added to the end of the settling chamber as shown in Figure 2.20. With a nominally linear relationship between force and compression, a stack height of 8 inches and minimum compression of 0.875 inches was chosen to produce a combined minimum force of 3000 pounds to always lift the upper nozzle block and keep the actuators in compression.

The four servo motors are each driven by individual servo drives powered by 240 VAC 3-phase. These four drives and servo motors are controlled synchronously by a programmable logic controller (PLC) through EtherCAT, the fastest industrial Ethernet communication protocol. The PLC

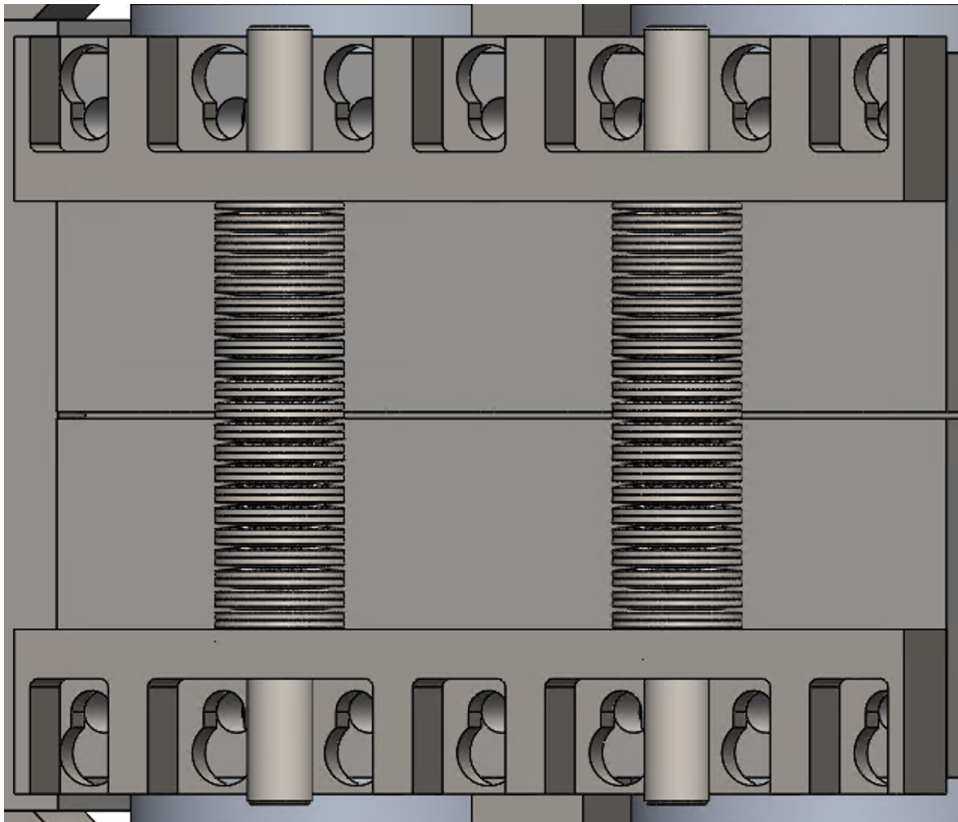


Figure 2.20: Inverted disc springs stacks at the end of the settling chamber.

logic programs are written in its associated software, Sysmac Studio. This software is a graphical ladder logic environment designed to integrate many automation devices across EtherCAT.

The specific program to control the Mach number will be created in future work. This program will initially be designed with four control objectives: (1) precise set Mach number, (2) Mach number sweep with specified start, stop, and time, (3) Mach number schedule, and (4) feedback-control for Mach number. The completed Mach number control program will be provided in Appendix C. Additionally, three analog modules were added to the PLC to input the static pressure, stagnation pressure, and temperature measured by the corresponding sensors to enable feedback-control.

Additional components of the system include two safety limit switches for each actuator, an external encoder for each actuator for additional physical feedback, various power supplies and relays, an emergency stop button, and a 7" human machine interface (HMI) for a simple control

interface that can be updated and expanded for any desired controls.

2.2.6.4 Final Overall Design

The final design with all modeled components is shown in Figure 2.21. The entire design will integrate with the existing ACE test section and other infrastructure. The overall length from the nozzle-test-section flange to the inlet of the 4-way manifold is 94 inches, shown in Figure 2.22, which is only around 12 inches longer than ACE.

2.2.6.5 FEA

The structural integrity of the final design was simulated using finite element analysis (FEA) in Solidworks. There were four primary simulations conducted: (1) lower nozzle and settling chamber at 200 psia with gravity, (2) upper nozzle and settling chamber at full vacuum with gravity, (3) sidewall with clamps at 200 psia, (4) and flexure fatigue at maximum deflection.

From all of these simulations, the minimum FOS achieved was 1.8. [Flexure fatigue results...](#)

[What figures to show? Show displacement plots? Can show setup with pressure and fixtures.](#)

[Resulting stress plots are not great to show.](#)

2.3 Fabrication Plans

[How much to detail? Pictures of stock? What parts to show final machined?](#)

All of the ACE2.0 parts are finished machining besides the nozzles, sidewalls, and brace. The fabrication is following the schedule shown in Figure 2.23, which shows the completed tasks in gray, the current tasks in green, orange, or red depending on status, and future tasks in white. The frame pieces were machined at the Texas A&M Fischer Engineering Design Center (FEDC) to utilize their water jet to cut the brace. An image of the brace after being cut out on the water jet is shown in Figure 2.24. The frame parts were originally planned to be water jet from the brace stock as well to save material cost and reduce excess as shown in Figure 2.25. It was later discovered that the cost of time and tooling on the water jet to cut all pieces from the 3 inch 4140 alloy steel is about the same as the cost of ordering 60 feet of bar stock. The decision to order the bar stock was made to allow the water jet to be used for other parts while the bar stock shipped and delivered.

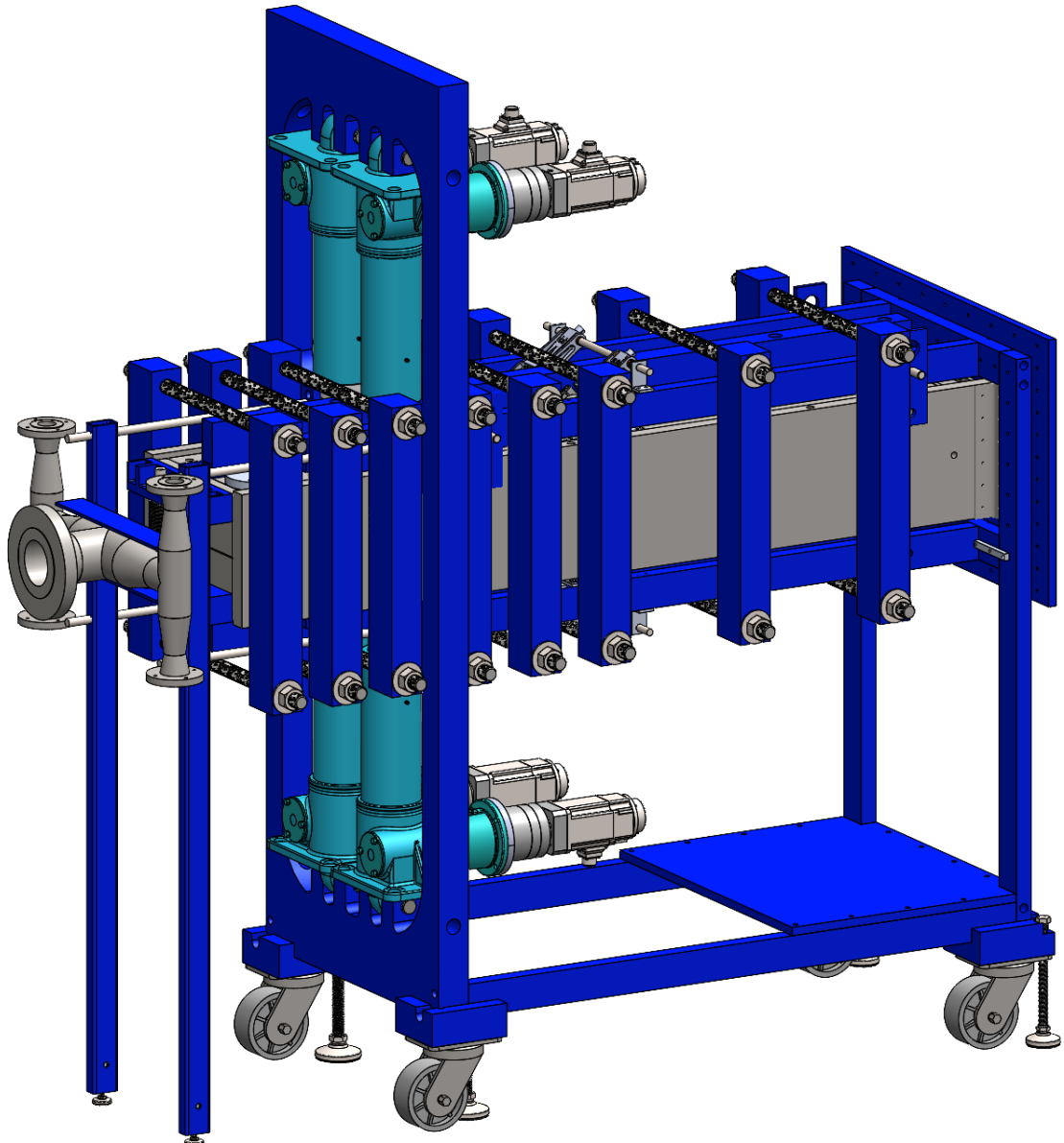


Figure 2.21: Full CAD model of ACE2.0 in Solidworks

The pallet of finished frame parts is shown in Figure 2.26.

The nozzles and sidewalls are currently being machined at Machine Works Inc. in Bryan, TX. The nozzles were first saw cut to a rough profile to minimize the amount of time on the CNC mill, as shown in Figure 2.27. They are currently being machined to a rough contour, and then the back of each will be machined flat prior to finishing the contour. For the final passes, the nozzle blocks

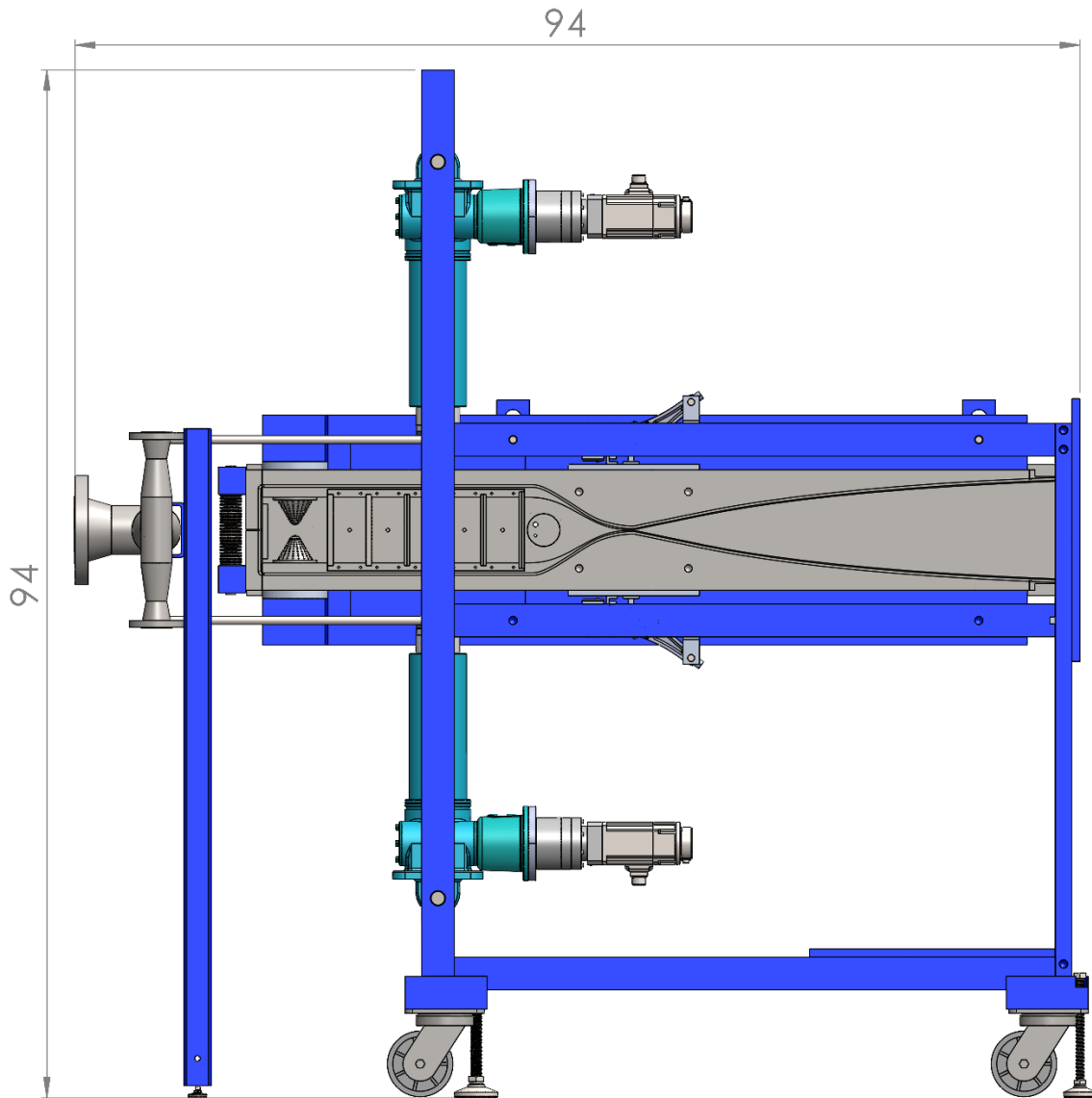


Figure 2.22: Side view of ACE2.0 in Solidworks

and flexures will be bolted together to ensure there is no step between the two pieces. Machine Works will also finish the brace for the frame by drilling and tapping holes.

The rest of the parts were machined at the Texas A&M Bush Combat Development Complex (BCDC). All of these parts are finished, but only the parts necessary for the pressure test have been picked up. BCDC will be the primary machine shop for any future fabrication throughout this work.

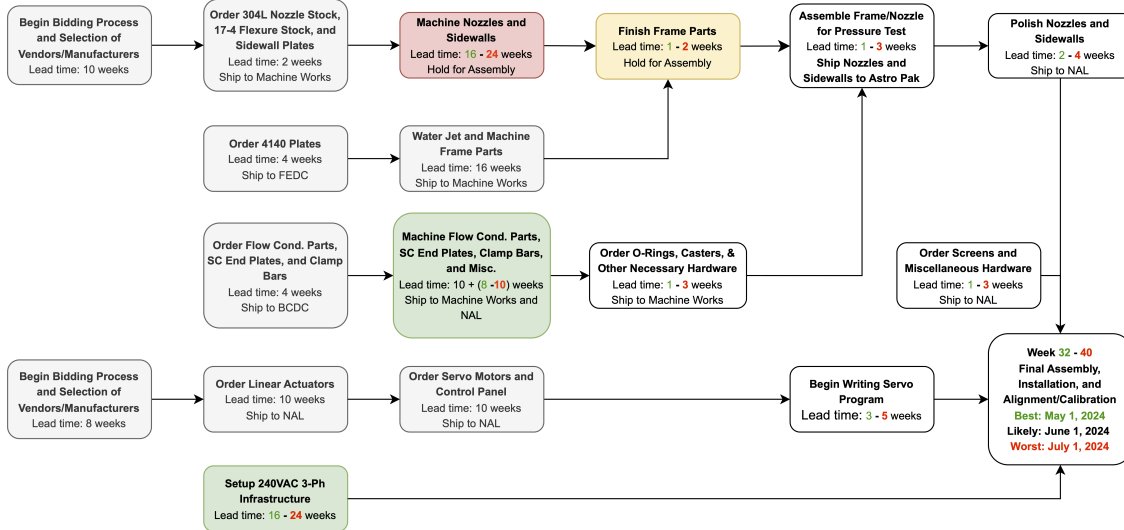


Figure 2.23: Manufacturing schedule beginning from September 25, 2023.



Figure 2.24: Rough cut brace on water jet.

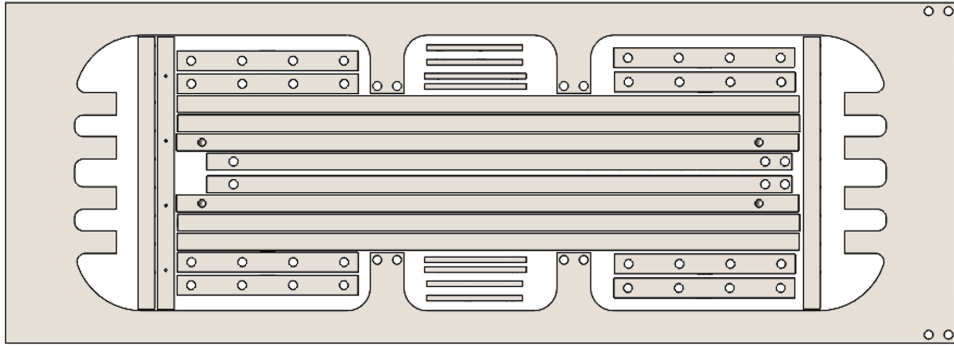


Figure 2.25: Planned water jet layout for frame parts.

2.3.1 Pressure Test

The hydro-pressure test will be performed at Machine Works prior to sending the nozzles and sidewalls to be polished. The base tunnel will be assembled with steel bars to simulate the actuators. The tunnel will be filled with water and pressurized to 200 psia for one hour, and the pressure will be monitored throughout. The primary goal of the pressure test is to ensure structural integrity at maximum pressure, but any major leaks will be addressed.

2.3.2 Polishing

Following the completion of the pressure test, the nozzles and sidewalls will be shipped to Astro Pak for polishing. All interior surfaces will be mechanically polished to a 1 Ra finish, and electropolishing will be used if necessary. In order to safely ship these pieces, the nozzle blocks will be assembled as shown in Figure 2.28 and custom wooden crates will be built.

2.4 Final Assembly, Installation, and Calibration

The final assembly will occur at the NAHL once the nozzle and sidewalls are delivered from polishing. Once nozzles and actuators are assembled in the frame, ACE2.0 will be rolled into the lab to replace ACE. All hoses, wires, and instrumentation attached to the nozzle and settling chamber will be removed and ACE will be rolled out of the lab. ACE2.0 will roll in and reconnect all hoses, wires, and instrumentation.

How to show assembly process?

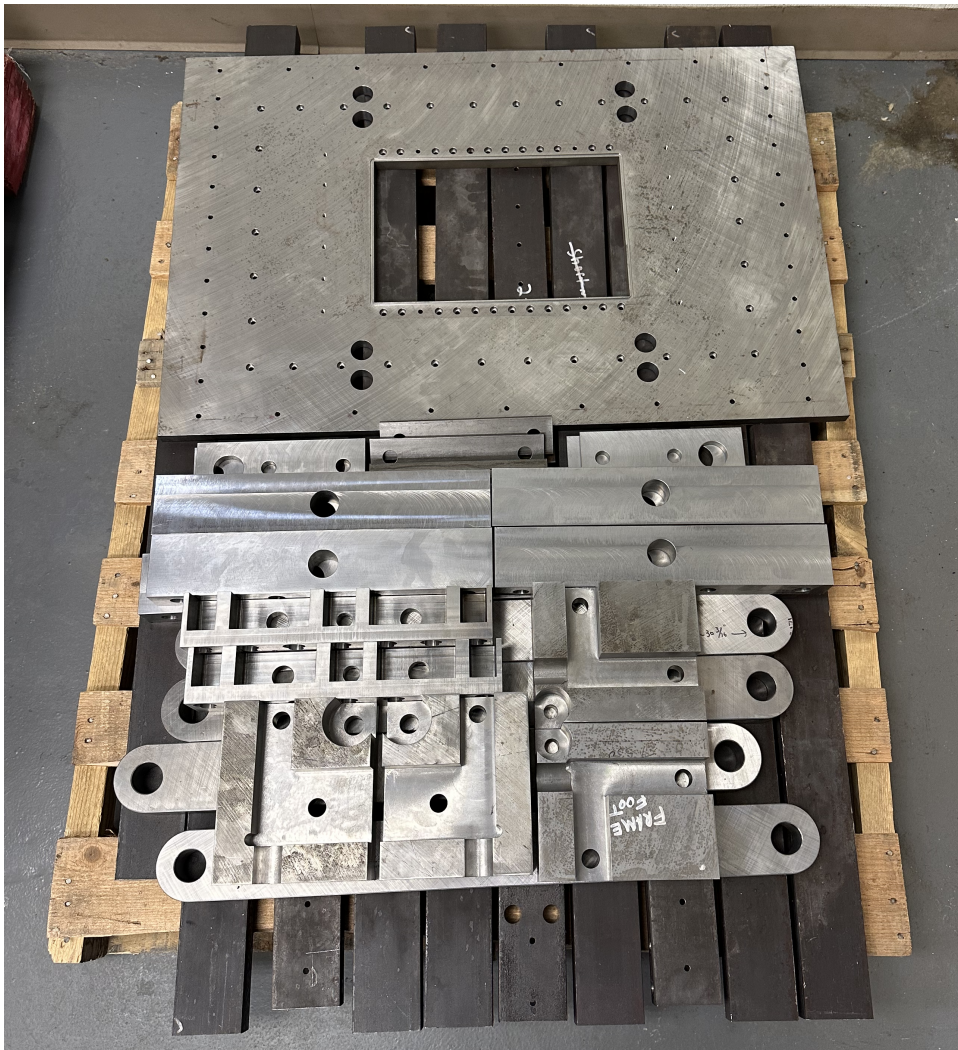


Figure 2.26: Pallet of finished frame parts from FEDC.

2.4.0.1 Nozzle Alignment

How to properly align and level nozzle?

2.4.1 Actuation Homing and Calibration

Before the sidewalls are installed, the nozzles will be actuated for homing the servo motors with the limit switches. At this point shims will be used to make fine adjustments to limit switch positions to ensure a minimum Mach number of 4.9 and a maximum Mach number of 8.5.



Figure 2.27: Nozzle block saw cut to rough profile.

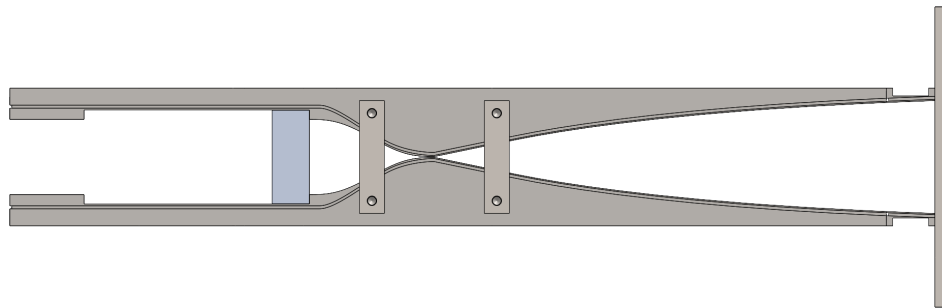


Figure 2.28: Nozzle assembly for shipping to polishing vendor.

2.4.2 Shakedown and First Runs

Decide what the first runs and measurements should be to properly calibrate.

3. EXPERIMENTAL APPROACH & OBJECTIVES

Following the completed installation and calibration discussed above, each of the three primary objectives will be accomplished or demonstrated sequentially. First, the improved experimental control and efficiency as a result of the above ACE2.0 design will be demonstrated by establishing and verifying the feedback-controlled active Mach variation and selection capability as well as the Reynolds number control scheme, if implemented. Second, the freestream flow produced by the calibrated nozzle will be characterized in terms of freestream flow uniformity and disturbance levels with uncertainty quantification and an exploration hysteresis. Third, the flow parameter control capabilities will be demonstrated in a proof of concept experiment of shock interactions during a Mach trajectory and any potential hysteresis exhibited. As a result of this work, the foundation will be set for future researchers to explore dynamic hypersonic aerodynamic in a more sophisticated and efficient manner with the control capabilities of ACE2.0.

3.1 Improved Experimental Control and Efficiency

The overall objective here is to establish and substantiate the mechanisms of ACE2.0 that allow greater control of the tunnel input parameters for both more efficient and dynamic experiments. The primary design objective of ACE2.0 was to enable active Mach number control during a run, which alone provides many key experimental advantages. However, there is still much to be desired with the parameter control capabilities to achieve full aerodynamic similarity for any flight trajectory. Thus, more precise control methods for Mach number and Reynolds number will be explored through the following objectives.

3.1.1 Feedback-Controlled Active Mach Number Variation and Selection

As stated, the primary design objective of ACE2.0 was to enable active control of the Mach number, but this capability will be taken one step further to accurately maintain the desired Mach number once set. During a tunnel run, the Mach number may vary because both pressure and thermal loads can cause the throat height to vary. Current experience shows that the Mach number

can vary by up to 5%. The goal of this work is to implement active feedback control and reduce this error to less than 0.5%.

The general approach for this feedback control is straightforward by designing a PID controller with an input of the measured Mach number and output of actuator position or velocity. The measured Mach number is calculated from the measured stagnation pressure and static pressure by solving the isentropic relation:

$$M = \sqrt{\frac{2}{\gamma - 1} \left[\left(\frac{P_0}{P} \right)^{\frac{\gamma-1}{\gamma}} - 1 \right]} \quad (3.1)$$

The relationship between the throat height and the Mach number is given by:

$$\frac{A^*}{A} = \frac{h^*}{h_{\text{exit}}} = M \left[\left(\frac{2}{\gamma + 1} \right) \left(1 + \frac{\gamma - 1}{2} M^2 \right) \right]^{-\frac{\gamma+1}{2(\gamma-1)}} \quad (3.2)$$

This is then subtracted from the set throat height to get the error signal for the PID transfer function:

$$E(s) = h_{\text{set}} - H(s) \quad (3.3)$$

There are many design options for PID controllers depending on the desired performance characteristics. The standard approach is simply a PI controller due to the derivative action amplifying measurement noise and potential causing instability [25]. However, the derivative effect of limiting overshoot and settling time is desirable, so it will not be neglected entirely. One final option is to add high frequency filtering into the derivative term to mitigate the effects of measurement noise. Each of these options will be explored, and the following equations show the transfer functions for

PI, PID, and PID with high frequency noise filtering respectively:

$$G(s) = \frac{H(s)}{E(s)} = K \left(1 + \frac{1}{T_i s} \right) \quad (3.4a)$$

$$= K \left(1 + \frac{1}{T_i s} + T_d s \right) \quad (3.4b)$$

$$= K \left(1 + \frac{1}{T_i s} + \frac{T_d s}{1 + \frac{T_d s}{N}} \right), \quad N = 2 \text{ to } 20 \quad (3.4c)$$

In practice, the Sysmac software used to write the logic for the PLC has a built-in PID function with gain autotuning capability. This will be explored in detail first in simulations in Sysmac followed by active tests in ACE2.0. This built-in PID loop will be used permanently if the resulting Mach number control is sufficient. Otherwise, the PID controller described above will be fully developed and implemented. In either case, a gain schedule will also be developed to modify the controller response throughout the Mach range to best handle the nonlinearity of the throat height and Mach number relationship.

3.1.2 Reynolds Number Control Scheme

In subscale model experiments, the Reynolds number plays an important role in maintaining similarity with real-world situations. Controlling the Reynolds number more effectively will enable more accurate and intentional experiments. The primary goal of this objective is to provide a feedback control scheme that allows the Reynolds number to be held at a set value that is either constant or dynamic. For the purposes of this discussion, any mention of the Reynolds number will be referring to the unit Reynolds number, $Re' = \frac{\rho U}{\mu}$.

The main control parameter for Reynolds number will be the settling chamber stagnation pressure. The Reynolds number is coupled with respect to pressure, temperature, and Mach number. The goal will be to control the stagnation pressure to counteract changes in both temperature and Mach number. For reference, the settling chamber stagnation temperature typically increases during a run by up to 40 K, and, of course, the Mach number can vary between 5 and 8. The effect of temperature will be examined during both simulations and experiments to determine if a more ad-

equate control system is required to maintain constant temperature or if this effect on the Reynolds number can be compensated by changing the pressure.

A mathematical model will be developed to be implemented for future physical PID control of the pressure regulator and the Reynolds number as a result. The physical implementation of this controller in this work will be dependent on budget and schedule constraints. The primary constraint here will be the ability to quickly replace the existing regulator manual valve control with a controlled valve. The M6QT utilizes the same air supply infrastructure, so any complications throughout the valve replacement process would result in both facilities being inoperable and a delay in all planned research for this work and others.

One other factor to be considered in the stagnation pressure control is the time response delay due to both the distance between the regulator and the tunnel and the maximum operating speed of the regulator. The distance from the regulator to the settling chamber inlet is around 7 meters, resulting in a maximum response time of 140 milliseconds with a minimum pipe flow velocity of $v_{pipe,min} = \dot{m}_{min}/\rho/A_{pipe} \approx 50 \frac{m}{s}$. The maximum regulator operating speed is...

I originally had given the sound speed and a much shorter time delay, but I changed it to this after talking with Drew about it. We can discuss when we meet.

The following derivation provides a starting point for the mathematical model.

begin{fix equations}

$$Re' = \frac{\rho U}{\mu} \quad (3.5)$$

$$\frac{T_0}{T} = \left(1 + \frac{\gamma - 1}{2} M^2\right) = F \quad (3.6)$$

$$\frac{P_0}{P} = \left(1 + \frac{\gamma - 1}{2} M^2\right)^{\frac{\gamma}{\gamma+1}} = F^{\frac{\gamma}{\gamma+1}} \quad (3.7)$$

$$\rho = \frac{P}{RT} = \frac{P_0 F^{\frac{-\gamma}{\gamma-1}}}{RT_0 F^{-1}} = \frac{P_0}{RT_0 F^{\frac{1}{\gamma-1}}} \quad (3.8)$$

$$U = M \sqrt{\gamma RT} = M F^{-\frac{1}{2}} \sqrt{\gamma RT_0} \quad (3.9)$$

$$Re' = \frac{\rho U}{\mu} = \frac{1}{\mu} \frac{P_0}{RT_0 F^{\frac{1}{\gamma-1}}} M F^{-\frac{1}{2}} \sqrt{\gamma RT_0}$$

$$Re' = \sqrt{\frac{\gamma}{RT_0}} \frac{MP_0}{\mu} F^{-\frac{\gamma+1}{2(\gamma-1)}} \quad (3.10)$$

Differentiating Re' assuming γ and R are constant and with $\frac{dF}{dt} = (\gamma - 1)M \frac{dM}{dt}$ gives:

$$\frac{d(Re')}{dt} = P_0 \frac{dM}{dt} + M \frac{dP_0}{dt} - \frac{MP_0}{\mu} \frac{d\mu}{dt} - \frac{\gamma+1}{2} M^2 P_0 F^{-1} \frac{dM}{dt} \quad (3.11)$$

Sutherland's Law with $T_\mu = 273$, $S_\mu = 111$, and $\mu_0 = 1.716 \times 10^{-5}$:

$$\mu = \mu_0 \frac{T_\mu + S_\mu}{T + S_\mu} \left(\frac{T}{T_\mu} \right)^{\frac{3}{2}} \quad (3.12)$$

$$\mu = \frac{\mu_0(T_\mu + S_\mu)}{T_\mu^{\frac{3}{2}}} \frac{T_0^{\frac{3}{2}} F^{-\frac{3}{2}}}{T_0 F^{-1} + S_\mu} \quad (3.13)$$

$$\frac{\frac{d\mu}{dt}}{\mu} = (\gamma - 1) M F^{-1} \frac{dM}{dt} \left(\frac{T_0 F^{-1}}{T_0 F^{-1} + S_\mu} - \frac{3}{2} \right) \quad (3.14)$$

Substituting and solving for $\frac{dP_0}{dt}$:

$$\frac{dP_0}{dt} = P_0 M F^{-1} \frac{dM}{dt} \left[(\gamma - 1) \left(\frac{T_0 F^{-1}}{T_0 F^{-1} + S_\mu} - \frac{3}{2} \right) + \frac{\gamma+1}{2} - \frac{1}{M^2 F^{-1}} \right] \quad (3.15)$$

end{fix equations}

Following the same logic as before, either a PI, PID, or PID with high frequency noise filtering will be implemented based on experimental results of Reynolds number control. However, in this case the calculated Reynolds number will be subtracted from the set condition to get the error signal and the controlled parameter will either be the stagnation pressure or the respective regulator position.

$$E(s) = Re'_{\text{set}} - Re'(s) \quad (3.16)$$

$$G(s) = \frac{P_0(s)}{E(s)} \text{ or } \frac{X(s)}{E(s)} = K \left(1 + \frac{1}{T_i s} \right) \quad (3.17a)$$

$$= K \left(1 + \frac{1}{T_i s} + T_d s \right) \quad (3.17b)$$

$$= K \left(1 + \frac{1}{T_i s} + \frac{T_d s}{1 + \frac{T_d s}{N}} \right), \quad N = 2 \text{ to } 20 \quad (3.17c)$$

At the very least, this model will be fully developed and simulated to ensure minimal future work for implementation. The physical control mechanism will also be explored and potentially purchased to allow install at the earliest convenience between the ACE2.0 and M6QT schedules.

3.2 Freestream Flow Uniformity and Disturbance Levels Characterization

In order to establish a baseline of performance characteristics for future work within the ACE2.0 facility, a pitot and hot-wire survey will be performed to measure and characterize the freestream flow uniformity and disturbance levels (noise) throughout the nozzle. The survey will utilize both a pitot rake and a single pitot probe with Kulite pressure transducers mounted on a traverse to characterize the pressure fluctuations and uniformity and a hot-wire anemometer to measure mass flux fluctuation levels.

A final noise survey was performed in ACE to establish a control for comparison with ACE2.0 as well as provide a preliminary exploration of noise hysteresis. The survey utilized a single pitot probe to measure the noise along the centerline at 6 and 24 inches upstream of the nozzle exit as shown in Figure 3.2. For each run, the Reynolds number was increased above the transition value ($Re' = 3 \times 10^6 / m$) discussed in the previous chapter and then decreased back down to the initial value below the transition value. These measurements provided baseline data for pressure fluctuation hysteresis. The results are shown in Figure 3.1. As seen, there is no discernible hysteresis in the freestream pressure fluctuation levels as the Reynolds number is swept up and back down. This survey will be repeated using a hot-wire anemometer to measure mass flux fluctuation levels if the remaining schedule for ACE permits.

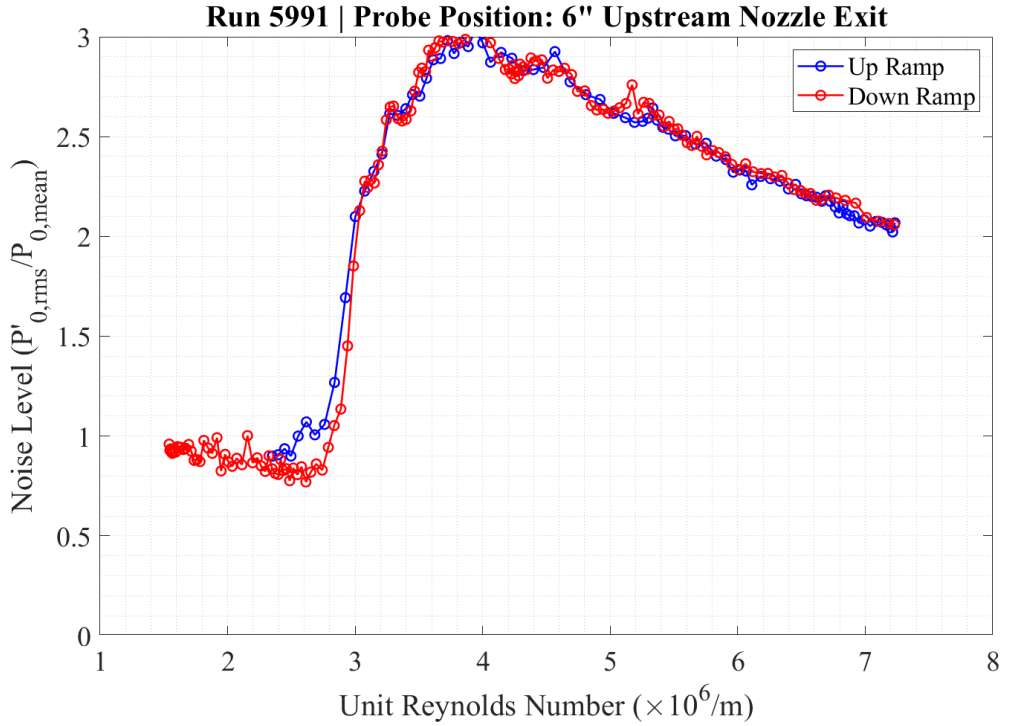


Figure 3.1: ACE freestream pressure fluctuations...

The anticipated characterization test matrix for ACE2.0 is shown in Table 3.1. The pitot rake will be used to characterize the freestream flow uniformity in the nozzle exit plane and a plane 6 inches upstream. The single pitot probe and hot-wire anemometer will be used to measure the freestream pressure fluctuation and mass flux fluctuation levels, respectively, along the centerline up to 24 inches upstream of the nozzle exit. The runs in each test matrix are divided into a few distinct objectives: (1) uniformity, (2) uncertainty quantification, (3) disturbance levels transition, and (4) hysteresis. The last five runs will be replicates of the first five to better quantify the uncertainty in Mach number, Reynolds number, and flow uniformity. This entire process will be documented so that flow-quality verification tests can be repeated as part of ongoing lab operations.

3.2.1 Freestream Uncertainty Quantification

The process to quantify the uncertainty of the various parameters for this work will closely follow Stephens's et al. [31] and Curriston's [32] approaches by simply focusing on establishing



Figure 3.2: Pitot probe measuring 24 inches upstream of nozzle exit.

a baseline for the uncertainty and making recommendations for improvement if necessary. The three steps to establish this baseline uncertainty for ACE2.0 will be (1) gather/measure systematic elemental uncertainties, (2) input into a Monte Carlo code along with data reduction equations to simulate systematic uncertainties, and (3) measure repeat data points through a few replicate experiments and calculate random uncertainties.

First, the systematic elemental uncertainties can be gathered and measured from the various sensors, which includes the static pressure transducer, stagnation pressure transducer, stagnation temperature thermocouple, and servo motor internal encoders. Each of these has a predefined manufacturer uncertainty that can be used, but some of these are very conservative and not ideal. The pressure sensors and temperature sensor will be tested against a working standard to measure the true uncertainty, which is often found to be an order of magnitude less than the manufacturer uncer-

Run	X (in.)	Y (in.)	Z (in.)	Mach	$Re' (10^6)$	Instrument
1	0	-3:1:3	0	6*	3*	Rake
2	0	-3:1:3	-3:1:3	8	3	Rake
3	0	-3:1:3	-3:1:3	7	3	Rake
4	0	-3:1:3	-3:1:3	6	3	Rake
5	0	-3:1:3	-3:1:3	5	3	Rake
6	-6	-3:1:3	-3:1:3	5	3	Rake
7	-6	-3:1:3	-3:1:3	6	3	Rake
8	-6	-3:1:3	-3:1:3	7	3	Rake
9	-6	-3:1:3	-3:1:3	8	3	Rake
10	0	0	0	8	$2 \rightarrow 7 \rightarrow 2$	Pitot
11	0	0	0	7	$2 \rightarrow 7 \rightarrow 2$	Pitot
12	0	0	0	6	$2 \rightarrow 7 \rightarrow 2$	Pitot
13	0	0	0	5	$2 \rightarrow 7 \rightarrow 2$	Pitot
14	0	0	0	$5 \rightarrow 8 \rightarrow 5$	3	Pitot
15	-6	0	0	$5 \rightarrow 8 \rightarrow 5$	3	Pitot
16	-6	0	0	5	$2 \rightarrow 7 \rightarrow 2$	Pitot
17	-6	0	0	6	$2 \rightarrow 7 \rightarrow 2$	Pitot
18	-6	0	0	7	$2 \rightarrow 7 \rightarrow 2$	Pitot
19	-6	0	0	8	$2 \rightarrow 7 \rightarrow 2$	Pitot
20	-17	0	0	6	$2 \rightarrow 7 \rightarrow 2$	Pitot
21	-17	0	0	$5 \rightarrow 8 \rightarrow 5$	3	Pitot
22	-24	0	0	$5 \rightarrow 8 \rightarrow 5$	3	Pitot
23	-24	0	0	6	$2 \rightarrow 7 \rightarrow 2$	Pitot
24-37	Repeat runs 10-23 with Hot-wire					
38-42	Replicate runs 1-5					

Table 3.1: Test matrix for ACE2.0 freestream characterization.

tainty [32]. The systematic uncertainty of any sensors utilized in future experiments is outside the scope of this work and must be considered when calculating the total uncertainty of measurements in each experiment.

Next, these systematic elemental uncertainties will be propagated through a Monte Carlo simulation along with the specific data reduction equations for the facility. This output will provide the total systematic uncertainty for each parameter of interest, which will be added to the random uncertainty to give the total uncertainty. Additionally, this simulation will also be used to provide a sensitivity analysis of the uncertainty to the various input parameters. This will be insightful on

how to best improve the uncertainty if necessary.

Finally, repeat data points will be measured by repeatedly settling on and off the set condition for the parameter of interest. While data will be gathered throughout the entire characterization test matrix, runs 1 and 20 will be solely for repeat data measurements. These two runs will provide a direct comparison of replicates that will account for any correlations that were not considered or unquantifiable. The standard deviation of this data will be added in quadrature to the systematic uncertainty to calculate the total uncertainty for each parameter of interest for the freestream flow.

3.2.2 Freestream Disturbance Hysteresis

Dynamic sweeps of both Mach number and Reynolds number will be performed to explore any potential hysteresis effects in either the noise or the control parameters. Specifically, this will be accomplished during the dynamic runs in the characterization test matrix in Table 3.1. The goal is simply to identify the existence of any hysteresis effects to inform future work within ACE2.0. The Reynolds number sweep runs are necessary to determine the value at which transition occurs, so sweeping the Reynolds number back down will not add any additional work and will ensure that there is no hysteresis. For the Mach number however, there is no past data to determine the existence of hysteresis, so these runs will establish a baseline. The noise level is known to decrease with an increase in Mach number, so identifying any hysteresis in this will be necessary to inform future experiments.

3.3 Mach Trajectory and Potential Hysteresis Proof of Concept Experiment

This objective will primarily serve as a demonstration of the capabilities for ACE2.0 and will also provide preliminary insight into the hysteretic behavior of dynamic Mach number experiments. The flow characteristic that will be specifically explored in this research will be shock interactions using schlieren. The goal will be to observe hysteresis in the transition from regular reflection to Mach reflection by varying the Mach number. The challenge of this is that the only facilities that have successfully produced this hysteresis had low freestream disturbance levels and an open-jet test section, while ACE2.0 has a closed test section and is not considered a "quiet"

facility. In order to provide the best conditions for hysteresis to be observed, these experiments will be performed at higher Mach numbers and a lower unit Reynolds number where freestream disturbance levels are lowest.

The experiments will be based on the methodologies and results from Durand et al. [15] and Tao et al. [45] in addition to the experimental setup of Mai [6]. The Mach number will be varied across either the Von Neumann condition or the detachments criteria to force the transition from regular reflection to Mach reflection or vice versa. In order to choose the wedge angle and Mach number range for each experiment, Figure 3.6 was created following the processes shown by Mouton [42] for each condition. The basic parameters across an oblique shock shown in Figure 3.3 are given as a function of the Mach number in region x (M_x), the shock angle (α), and the ratio of specific heats (γ).

Too much in the weeds. Reword as just process without all the equations

The pressure ratio is

$$\xi(M_x, \alpha) = \frac{P}{P_x} = \frac{2\gamma M_x^2 \sin^2 \alpha - (\gamma - 1)}{\gamma + 1} \quad (3.18)$$

The flow deflection angle (wedge angle) and Mach number are given as

$$\theta(M_x, \alpha) = \cot^{-1} \left[\left(\frac{(\gamma + 1)M_x^2}{2(M_x^2 \sin^2 \alpha - 1)} \right) \tan \alpha \right] \quad (3.19)$$

$$M(M_x, \alpha) = \sqrt{\frac{(\gamma + 1)^2 M_x^4 \sin^2 \alpha - 4(M_x^2 \sin^2 \alpha - 1)(\gamma M_x^2 \sin^2 \alpha + 1)}{[2\gamma M_x^2 \sin^2 \alpha - (\gamma - 1)][(\gamma - 1)M_x^2 \sin^2 \alpha + 2]}} \quad (3.20)$$

The shock angle when the flow deflection angle is maximum is given by setting $\frac{\partial \theta}{\partial \alpha} = 0$, resulting in

$$\alpha^{\theta_{max}}(M_x) = \sin^{-1} \sqrt{(\gamma + 1) \frac{M_x^2 - \frac{4}{\gamma+1} + \sqrt{M_x^4 + 8\frac{\gamma-1}{\gamma+1}M_x^2 + \frac{16}{\gamma+1}}}{4\gamma M_x^2}} \quad (3.21)$$

For the detachment condition shown in Figure 3.3

$$M_{1,D} = M(M_\infty, \alpha_D) \quad (3.22)$$

$$\theta(M_\infty, \alpha_D) = \theta(M_{1,D}, \alpha^{\theta_{max}}(M_{1,D})) \quad (3.23)$$

Solving this for α_D results in a fifth-order polynomial in $\sin^2 \alpha_D$

$$D_0 + D_1 \sin^2 \alpha_D + D_2 \sin^4 \alpha_D + D_3 \sin^6 \alpha_D + D_4 \sin^8 \alpha_D + D_5 \sin^{10} \alpha_D = 0 \quad (3.24)$$

where

$$D_0 = -16$$

$$D_1 = 32M_\infty^2 - 4M_\infty^4 - 48M_\infty^2\gamma - 16M_\infty^4\gamma + 16\gamma^2 - 16M_\infty^4\gamma^2$$

$$+ 16M_\infty^2\gamma^3 + 4M_\infty^4\gamma^4$$

$$D_2 = -16M_\infty^4 + 4M_\infty^6 - M_\infty^8 + 104M_\infty^4\gamma + 16M_\infty^6\gamma - 4M_\infty^8\gamma$$

$$- 64M_\infty^2\gamma^2 - 32M_\infty^4\gamma^2 + 8M_\infty^6\gamma^2 - 6M_\infty^8\gamma^2 - 56M_\infty^4\gamma^3$$

$$- 16M_\infty^6\gamma^3 - 4M_\infty^8\gamma^3 - 12M_\infty^6\gamma^4 - M_\infty^8\gamma^4$$

$$D_3 = M_\infty^8 - 64M_\infty^6\gamma + 4M_\infty^8\gamma + 96M_\infty^4\gamma^2 + 64M_\infty^6\gamma^2 + 14M_\infty^8\gamma^2$$

$$+ 64M_\infty^6\gamma^3 + 20M_\infty^8\gamma^3 + 9M_\infty^8\gamma^4$$

$$D_4 = 8M_\infty^8\gamma - 64M_\infty^6\gamma^2 - 32M_\infty^8\gamma^2 - 24M_\infty^8\gamma^3$$

$$D_5 = 16M_\infty^8\gamma^2$$

This equation is solved numerically for Mach numbers greater than unity, and only one solution for each $\sin^2 \alpha_D$ exists that is real and bounded between zero and one. The values of $\theta_D(M) = \theta(M_\infty, \alpha_D)$ solved for freestream Mach numbers from 2 to 9 yields the upper curve in Figure 3.6.

For the Von Neumann condition shown in Figure 3.4

$$M_{1,V} = M(M_\infty, \alpha_V) \quad (3.25)$$

$$\xi\left(M_\infty, \frac{\pi}{2}\right) = \xi(M_\infty, \alpha_V) \xi(M_{1,V}, \alpha_{1,V}) \quad (3.26)$$

$$\frac{2\gamma M_{1,V}^2 \sin^2 \alpha_{1,V} - (\gamma - 1)}{\gamma + 1} = \frac{\xi(M_\infty, \frac{\pi}{2})}{\xi(M_\infty, \alpha_V)} \quad (3.27)$$

$$\alpha_{1,V} = \sin^{-1} \sqrt{\frac{(\gamma - 1) + (\gamma + 1) \frac{\xi(M_\infty, \frac{\pi}{2})}{\xi(M_\infty, \alpha_V)}}{2\gamma M_{1,V}^2}} \quad (3.28)$$

The solution for $\alpha_{1,V}$ is found numerically by solving the equation

$$\theta(M_\infty, \alpha_V) = \theta(M_{1,V}, \alpha_{1,V}) \quad (3.29)$$

The values of $\theta_V(M) = \theta(M_\infty, \alpha_V)$ solved for freestream Mach numbers from 2.2 to 9 yields the lower curve in Figure 3.6.

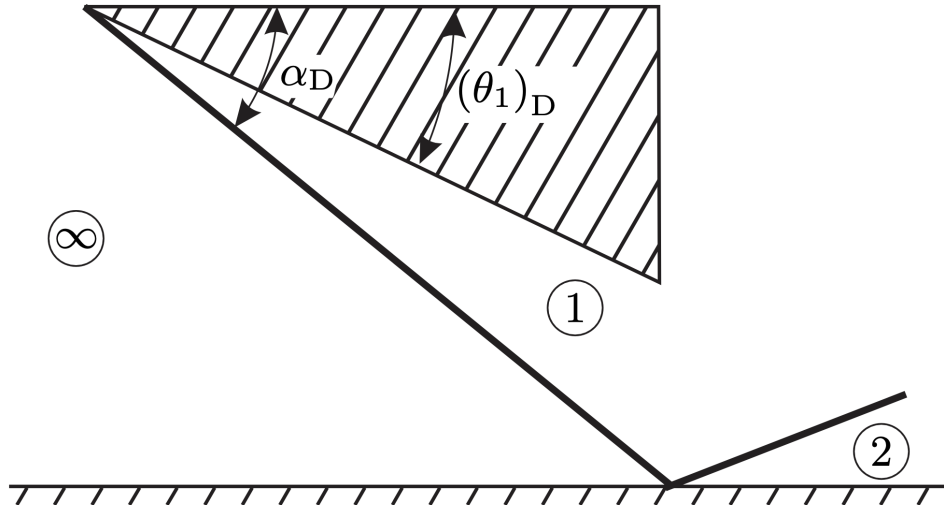


Figure 3.3: Flow over wedge resulting in regular reflection of shock [42]

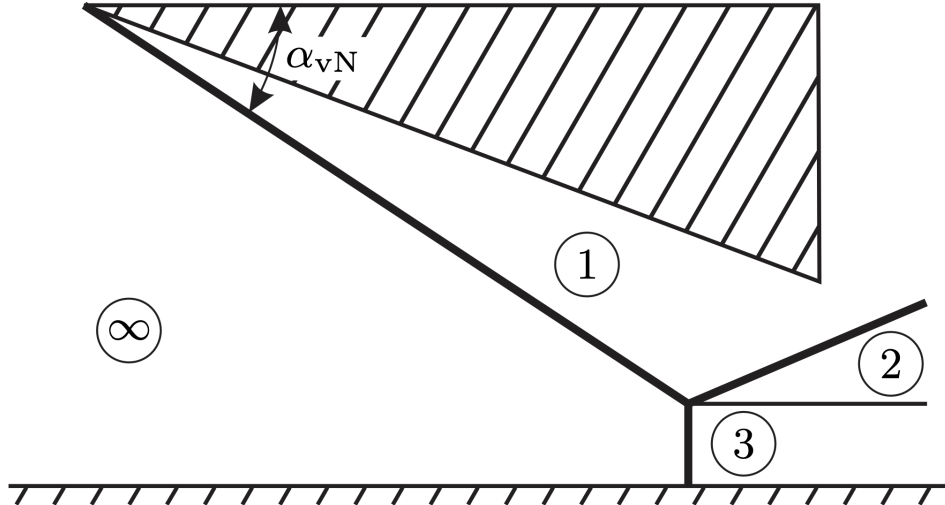


Figure 3.4: Flow over wedge resulting in Mach reflection of shock [42]

The two experimental setups are shown as A and B. For A, the wedge angle is 30° and the Mach number range is 7 to 8. For B, the wedge angle is 20.3° and the Mach number range is 6 to 8. For both paths, the Mach number will start at the point in the dual solution domain, decrease across either the detachment condition or the Von Neumann condition, and then increase back into the dual solution domain (i.e. AA'A, BB'B). The reverse of these will also be explored if hysteresis is not observed initially.

The physical model for these experiments will be very similar to the double wedge setup used by Mai [6] in ACE as shown in Figure 3.5. If 3D printing with Rigid 10K produces an acceptable leading edge, then a pair will be printed for each angle needed. If future research will utilize this double wedge setup, then a hinged mechanism will be designed and fabricated to use a single pair of wedges for any desired angle.

The expected results should appear similar to the numerical results from Ben-Dor et al. [37], Durand et al. [15], and Tao et al. [45] with an example shown in Figure 3.7. Although the Mach number range and wedge angle are different, the hysteresis should be the same for the chosen paths in this experiment. The path in Figure 3.7 is representative of path AA'A, which crosses the detachment condition. There have not been any simulations published that cross the Von Neumann

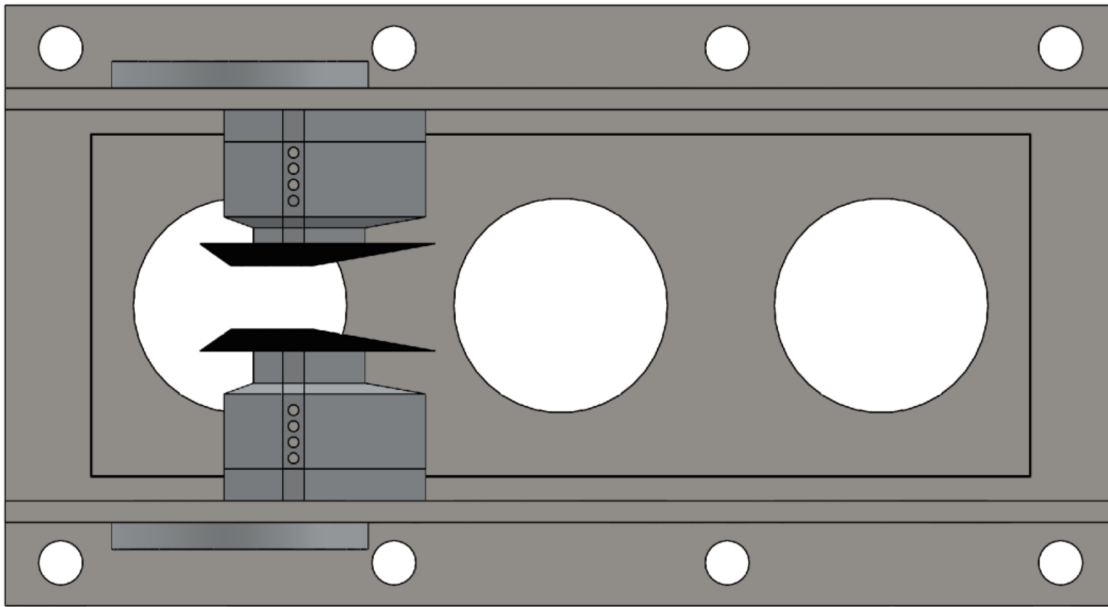


Figure 3.5: Double wedge setup [6]

condition by varying the Mach number, so path B will be explored secondary to path A.

In either case, the final objective will be to guide future experiments by determining if ACE2.0 is capable of reproducing the hysteresis in shock interactions or incapable due to freestream noise.

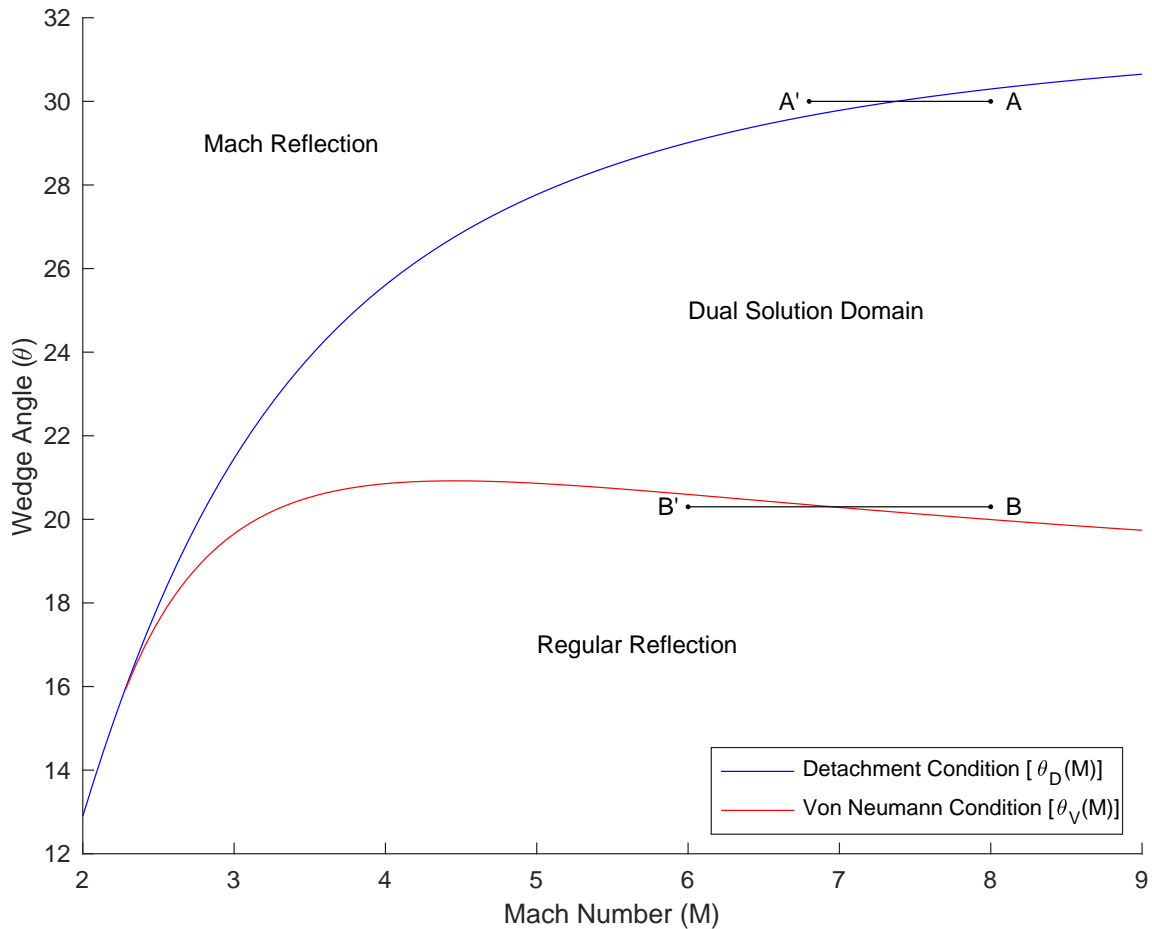


Figure 3.6: Shock wave reflection configuration domains for Mach number and wedge angle.

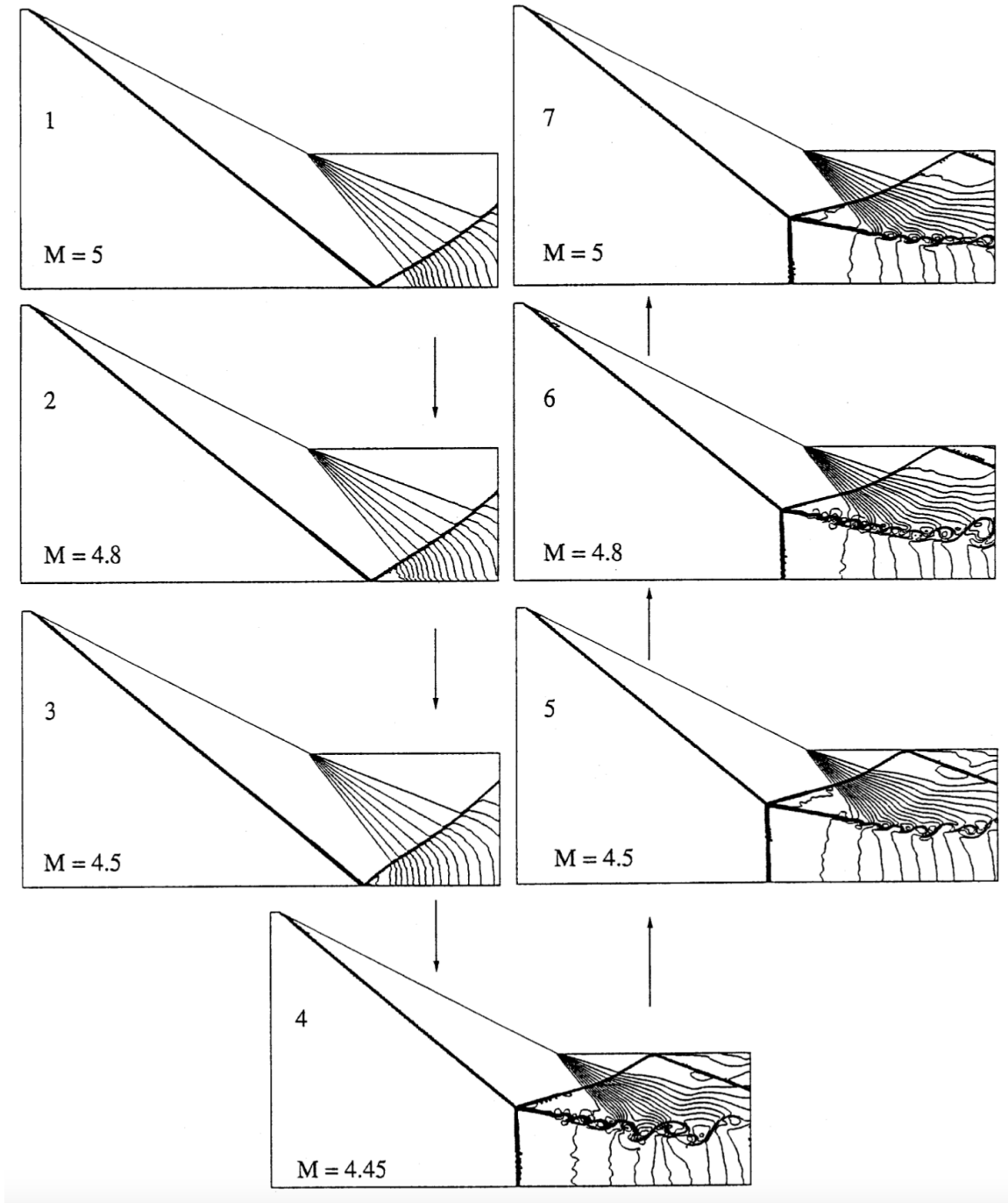


Figure 3.7: Mach-number-variation-induced hysteresis for 27° wedge [37]

4. REAMAINING WORK

The path forward will follow the manufacturing schedule shown in Figure 2.23. The pressure test will be performed as soon as the nozzles are finished machining, tentatively May 1, 2024. Depending on the results of the pressure test, the process could be anywhere from a single day to two weeks. Once complete though, the nozzles and sidewalls will be shipped to the polishing vendor, which should have a quick turn around of two weeks. Upon arrival to the NAHL, the full ACE2.0 nozzle will be finally assembled and installed. With proper planning prior to the final installation, the process should not take more than a week to begin shakedown and characterization.

In the meantime, the servo control program will be written between now and the final nozzle machining. The Mach number feedback will be implemented, and the Reynolds number control capability will be explored and potentially implemented before the final install. Again, this will primarily depend on the test schedule for the M6QT and the amount of time needed to replace the manual valve with a controlled valve.

The characterization and hysteresis experiments will be performed immediately following installation and initial calibration. The primary goal is to ensure complete function of ACE2.0 along with a demonstration of the capabilities and potential for future research. Additionally, the documentation for the nozzle operation will be written based on the best practices deduced throughout the experiments.

4.1 Maybe

Might have another section

4.2 Possibly

Could possibly have another section

REFERENCES

- [1] I. A. Leyva, “The relentless pursuit of hypersonic flight,” *Physics Today*, vol. 70, pp. 30–36, 11 2017.
- [2] M. Semper, N. Tichenor, R. Bowersox, R. Srinivasan, and S. North, *On the Design and Calibration of an Actively Controlled Expansion Hypersonic Wind Tunnel*.
- [3] N. Tichenor, M. Semper, R. Bowersox, R. Srinivasan, and S. North, *Calibration of an Actively Controlled Expansion Hypersonic Wind Tunnel*.
- [4] N. Tichenor, *Characterization of the Influence of a Favorable Pressure Gradient on the Basic Structure of a Mach 5.0 High Reynolds Number Supersonic Turbulent Boundary Layer*. Doctoral dissertation, Texas A&M University, 2010.
- [5] M. Semper, B. Pruski, and R. Bowersox, *Freestream Turbulence Measurements in a Continuously Variable Hypersonic Wind Tunnel*.
- [6] C. Mai, *Near-Region Modification of Total Pressure Fluctuations by a Normal Shock Wave in a Low-Density Hypersonic Wind Tunnel*. Doctoral dissertation, Texas A&M University, 2014.
- [7] I. Neel, *Influence of Environmental Disturbances on Hypersonic Crossflow Instability on the HIFiRE-5 Elliptic Cone*. Doctoral dissertation, Texas A&M University, 2019.
- [8] A. N. Leidy, *An Experimental Characterization of 3-D Transitional Shock Wave Boundary Layer Interactions at Mach 6*. PhD thesis, 2019.
- [9] J. T. Kenney and L. M. Webb, “A summary of the techniques of variable mach number supersonic wind tunnel nozzle design,” *AGARDograph*, no. 3, 1954.
- [10] J. Rosen, “The design and calibration of a variable mach number nozzle,” *Journal of the Aeronautical Sciences*, vol. 22, no. 7, pp. 484–490, 1955.

- [11] S. F. Erdmann, “A new economic flexible nozzle for supersonic wind tunnels,” *Journal of Aircraft*, vol. 8, no. 1, pp. 58–60, 1971.
- [12] J. Rom and I. Etsion, “Improved flexible supersonic wind-tunnel nozzle operated by a single jack.,” *AIAA Journal*, vol. 10, no. 12, pp. 1697–1699, 1972.
- [13] B. Ilic, M. Milos, M. Milosavljevic, and J. Isakovic, “Model-based stagnation pressure control in a supersonic wind tunnel,” *FME Transaction*, vol. 44, pp. 1–9, 01 2016.
- [14] A. N. Shahrabaki, M. Bazazzadeh, M. D. Manshadi, and A. Shahriari, “Designing a fuzzy logic controller for the reynolds number in a blowdown supersonic wind tunnel,” *2014 IEEE Aerospace Conference*, pp. 1–12, 2014.
- [15] A. Durand, B. Chanetz, R. Benay, and A. Chpoun, “Investigation of shock waves interference and associated hysteresis effect at variable-mach-number upstream flow,” *Shock Waves*, vol. 12, p. 469–477, May 2003.
- [16] L. Laguarda, J. Santiago Patterson, F. F. Schrijer, B. W. van Oudheusden, and S. Hickel, “Experimental investigation of shock–shock interactions with variable inflow mach number,” *Shock Waves*, vol. 31, p. 457–468, Jul 2021.
- [17] P. Chen, F. Wu, J. Xu, X. Feng, and Q. Yang, “Design and implementation of rigid-flexible coupling for a half-flexible single jack nozzle,” *Chinese Journal of Aeronautics*, vol. 29, no. 6, pp. 1477–1483, 2016.
- [18] S.-g. Guo, Z.-g. Wang, and Y.-x. Zhao, “Design of a continuously variable mach-number nozzle,” *Journal of Central South University*, vol. 22, p. 522–528, Feb 2015.
- [19] Z. Lv, J. Xu, F. Wu, P. Chen, and J. Wang, “Design of a variable mach number wind tunnel nozzle operated by a single jack,” *Aerospace Science and Technology*, vol. 77, pp. 299–305, 2018.
- [20] W. Qi, J. Xu, and Z. Fan, *Design and Experimental Calibration of the Profile Rotating Wind Tunnel with Mach Number Varying from 2.0 to 4.0*.

- [21] C. A. Steeves, K. H. Timpano, P. T. Maxwell, L. Martinelli, and R. B. Miles, “Design and manufacture of a morphing structure for a shape-adaptive supersonic wind tunnel nozzle,” *Journal of Applied Mechanics*, vol. 76, no. 3, p. 031012, 2009.
- [22] D. Kraft, “Optimal control of a high performance wind tunnel,” *IFAC Proceedings Volumes*, vol. 18, no. 2, pp. 233–234, 1985. 5th IFAC Workshop on Control Applications of Nonlinear Programming and Optimization, Capri, Italy, Capri, Italy.
- [23] D.-S. Hwang and P.-L. Hsu, “A robust controller design for supersonic intermittent blowdown-type windtunnels,” *The Aeronautical Journal*, vol. 102, no. 1013, p. 161–170, 1998.
- [24] J. Matsumoto, F. Lu, and D. Wilson, “Pre-programmed controller for a supersonic blowdown tunnel,” 01 2001.
- [25] Y. T. Fung, G. Settles, and A. Ray, *Microprocessor Control of High-Speed Wind Tunnel Stagnation Pressure*.
- [26] B. Ilić, M. Miloš, and J. Isaković, “Cascade nonlinear feedforward-feedback control of stagnation pressure in a supersonic blowdown wind tunnel,” *Measurement*, vol. 95, pp. 424–438, 2017.
- [27] M. G. Silva, V. O. Gamarra, and V. Koldaev, “Control of reynolds number in a high speed wind tunnel,” *Journal of Aerospace Technology and Management*, vol. 1, pp. 69–77, 2009.
- [28] C. Nott, S. Ölçmen, D. Lewis, and K. Williams, “Supersonic, variable-throat, blow-down wind tunnel control using genetic algorithms, neural networks, and gain scheduled pid,” *Appl. Intell.*, vol. 29, pp. 79–89, 08 2008.
- [29] A. Chou, A. Leidy, R. A. King, B. F. Bathel, and G. Herring, *Measurements of Freestream Fluctuations in the NASA Langley 20-Inch Mach 6 Tunnel*.
- [30] L. Duan, M. M. Choudhari, A. Chou, F. Munoz, R. Radespiel, T. Schilden, W. Schröder, E. C. Marineau, K. M. Casper, R. S. Chaudhry, G. V. Candler, K. A. Gray, and S. P. Schnei-

- der, “Characterization of freestream disturbances in conventional hypersonic wind tunnels,” *Journal of Spacecraft and Rockets*, vol. 56, no. 2, pp. 357–368, 2019.
- [31] J. Stephens, E. Hubbard, J. Walter, and T. McElroy, “Uncertainty analysis of the nasa glenn 8x6 supersonic wind tunnel,” tech. rep., 2016.
- [32] D. Curriston, *Wind Tunnel Data Quality Assessment and Improvement Through Integration of Uncertainty Analysis in Test Design*. Doctoral dissertation, Texas A&M University, 2024.
- [33] H. G. Hornung, H. Oertel, and R. J. Sandeman, “Transition to mach reflexion of shock waves in steady and pseudosteady flow with and without relaxation,” *Journal of Fluid Mechanics*, vol. 90, no. 3, p. 541–560, 1979.
- [34] H. G. Hornung and M. L. Robinson, “Transition from regular to mach reflection of shock waves part 2. the steady-flow criterion,” *Journal of Fluid Mechanics*, vol. 123, p. 155–164, 1982.
- [35] A. Chpoun and G. Ben-Dor, “Numerical confirmation of the hysteresis phenomenon in the regular to the mach reflection transition in steady flows,” *Shock Waves*, vol. 5, pp. 199–203, 1995.
- [36] M. Ivanov, G. Ben-Dor, T. Elperin, A. Kudryavtsev, and D. Khotyanovsky, “Flow-mach-number-variation-induced hysteresis in steady shock wave reflections,” *AIAA journal*, vol. 39, no. 5, pp. 972–974, 2001.
- [37] G. Ben-Dor, M. Ivanov, E. Vasilev, and T. Elperin, “Hysteresis processes in the regular reflection mach reflection transition in steady flows,” *Progress in Aerospace Sciences*, vol. 38, no. 4-5, pp. 347–387, 2002.
- [38] G. Ben-Dor and G. Ben-Dor, *Shock wave reflection phenomena*, vol. 2. Springer, 2007.
- [39] A. Chpoun, D. Passerel, H. Li, and G. Ben-Dor, “Reconsideration of oblique shock wave reflections in steady flows. part 1. experimental investigation,” *Journal of Fluid Mechanics*, vol. 301, p. 19–35, 1995.

- [40] H. LI, A. CHPOUN, and G. BEN-DOR, “Analytical and experimental investigations of the reflection of asymmetric shock waves in steady flows,” *Journal of Fluid Mechanics*, vol. 390, p. 25–43, 1999.
- [41] M. S. Ivanov, A. N. Kudryavtsev, S. B. Nikiforov, D. V. Khotyanovsky, and A. A. Pavlov, “Experiments on shock wave reflection transition and hysteresis in low-noise wind tunnel,” *Physics of Fluids*, vol. 15, pp. 1807–1810, 06 2003.
- [42] C. A. Mouton, *Transition between regular reflection and Mach reflection in the dual-solution domain*. PhD thesis, California Institute of Technology, 2007.
- [43] T. Setoguchi, S. Matsuo, M. Ashraful Alam, J. Nagao, and H. D. Kim, “Hysteretic phenomenon of shock wave in a supersonic nozzle,” *Journal of Thermal Science*, vol. 19, pp. 526–532, 2010.
- [44] B. Chanetz and R. Benay, “Hysteresis phenomena associated with shock waves interference in steady hypersonic flow,” *International Journal of Aerodynamics*, vol. 2, no. 2-4, pp. 294–315, 2012.
- [45] Y. Tao, X. Fan, and Y. Zhao, “Viscous effects of shock reflection hysteresis in steady supersonic flows,” *Journal of fluid mechanics*, vol. 759, pp. 134–148, 2014.
- [46] K. Sabnis, D. Galbraith, H. Babinsky, and J. A. Benek, *The Influence of Nozzle Geometry on Corner Flows in Supersonic Wind Tunnels*.
- [47] W. S. Saric, “Görtler vortices,” *Annual Review of Fluid Mechanics*, vol. 26, no. 1, pp. 379–409, 1994.
- [48] E. Reshotko, W. Saric, and H. Nagib, “Flow quality issues for large wind tunnels,” *35th Aerospace Sciences Meeting and Exhibit*, Jan 1997.
- [49] W. F. Hilton, “High speed wind tunnel testing. a. pope and k. l. goin. john wiley & sons, london. 1965. 474 pp. illustrations. 115s.,” *The Aeronautical Journal*, vol. 70, no. 667, p. 739–739, 1966.

- [50] J. Anderson, *Fundamentals of Aerodynamics*. McGraw-Hill series in aeronautical and aerospace engineering, McGraw-Hill Education, 2017.
- [51] J. Anderson, *Modern Compressible Flow: With Historical Perspective*. Aeronautical and Aerospace Engineering Series, McGraw-Hill Education, 2021.

APPENDIX A

ACE2.0 NOZZLE CONTOUR

Code and equations to produce contour

Before:

```
do 10 i=1, nch
    theta(i) = dthetai + float(i-1)*dth
    x(i) = tan(theta(i))/2./k
    xw(i) = x(i)
    y(i) = 1.0 + k*x(i)**2
    yw(i) = y(i)
10 continue
```

After:

```
do 10 i=1, nch
    theta(i) = dthetai + float(i-1)*dth
    xthetai = sqrt(tan(thetai)/k)
    k4 = -k/2./xthetai
    pc = -9.*(k**2)/3./((4.*k4)**2)
    qc = (2.* (3.*k)**3 - 27.* ((4.*k4)**2)*tan(theta(i)))
& /27./((4.*k4)**3)
    npi = 2.*pi/3.
    tc = 2.*sqrt(-pc/3.)
& *cosacos((3.*qc/2./pc)*sqrt(-3./pc))/3. - npi)
    if((3.*qc/2./pc)*sqrt(-3./pc).lt.-1.) then
        tc = 2.*sqrt(-pc/3.)*cosacos(-1.)/3. - npi)
    end if
    x(i) = tc - k/4./k4
    xw(i) = x(i)
    y(i) = 1.0 + k*x(i)**3 + k4*x(i)**4
    yw(i) = y(i)
10 continue
```

The equations for each section are given by the following (in inches):

Subsonic: $-0.000267975228779994x^5 - 0.0066993807195x^4 - 0.04466253813x^3 + 0.033746187$

for $-10 < x < 0$

Throat: $-2689.610971179115x^4 + 181.528229581324x^3 + 0.033746187$ *for* $0 < x < 0.033746187$

Straight: $0.206725280364801x + 0.030258092015591$ *for* $0.033746187 < x < 6.1460114$

Straightening: $2.180909737850381x^{0.960492634168194} + 5.934566177927477 \times 10^{284}x^{-367.9331632104439}$
 $-1.684363604007221x^{1.011336503949665} - 0.023814395465567 \ln(0.418646933043039x)$
 -0.585293189697896 for $6.1460114 < x < 40.07774$



Figure A.1: A caption here

APPENDIX B

CFD RESULTS

The following figures show the full results compared between ACE and ACE2.0.



Figure B.1: A caption here

APPENDIX C

ACTUATION SPECIFICATIONS

Text for the Appendix follows.



Figure C.1: A caption here

C.1 Detailed Parts Lists and Descriptions

List of parts with descriptions where necessary...

C.2 Mach Number Control Program

The full servo motor control program in Sysmac will be displayed and described here.

APPENDIX D
TUNNEL INFRASTRUCTURE

Text for the Appendix follows.



Figure D.1: A caption here

APPENDIX E
OPERATING PROCEDURES

Text for the Appendix follows.



Figure E.1: A caption here

APPENDIX F

DETAILED FABRICATION DETAILS

Text for the Appendix follows.



Figure F.1: A caption here